The Astronomical Journal, 131:1648–1666, 2006 March

USING LINE PROFILES TO TEST THE FRATERNITY OF TYPE Ia SUPERNOVAE AT HIGH AND LOW REDSHIFTS[1]

Stéphane Blondin,[2] Luc Dessart,[3] Bruno Leibundgut,[2] David Branch,[4] Peter Höflich,[5] John L. Tonry,[6] Thomas Matheson,[7] Ryan J. Foley,[8] Ryan Chornock,[8] Alexei V. Filippenko,[8] Jesper Sollerman,[9] Jason Spyromilio,[2] Robert P. Kirshner,[10] W. Michael Wood-Vasey,[10] Alejandro Clocchiatti,[11] Claudio Aguilera,[12] Brian Barris,[6] Andrew C. Becker,[13] Peter Challis,[10] Ricardo Covarrubias,[13] Tamara M. Davis,[14] Peter Garnavich,[15] Malcolm Hicken,[10,16] Saurabh Jha,[8] Kevin Krisciunas,[15] Weidong Li,[8] Anthony Miceli,[13] Gajus Miknaitis,[17] Giuliano Pignata,[11] Jose Luis Prieto,[18] Armin Rest,[12] Adam G. Riess,[19] Maria Elena Salvo,[14] Brian P. Schmidt,[14] R. Chris Smith,[11] Christopher W. Stubbs,[10,16] and Nicholas B. Suntzeff[11]

Received 2005 August 5; accepted 2005 October 4

ABSTRACT

Using archival data of low-redshift ($z < 0.01$; Center for Astrophysics and SUSPECT databases) Type Ia supernovae (SNe Ia) and recent observations of high-redshift ($0.16 < z < 0.64$) SNe Ia, we study the "uniformity" of the spectroscopic properties of nearby and distant SNe Ia. We find no difference in the measurements we describe here. In this paper we base our analysis solely on line-profile morphology, focusing on measurements of the velocity location of maximum absorption ($v_{\rm abs}$) and peak emission ($v_{\rm peak}$). Our measurement technique makes it easier to compare low and high signal-to-noise ratio observations. We also quantify the associated sources of error, assessing the effect of line blending with assistance from the parameterized code SYNOW. We find that the evolution of $v_{\rm abs}$ and $v_{\rm peak}$ for our sample lines (Ca II λ3945, Si II λ6355, and S II $\lambda\lambda$5454, 5640) is similar for both the low- and high-redshift samples. We find that $v_{\rm abs}$ for the weak S II $\lambda\lambda$5454, 5640 lines and $v_{\rm peak}$ for S II λ5454 can be used to identify fast-declining [$\Delta m_{15}(B) > 1.7$] SNe Ia, which are also subluminous. In addition, we give the first direct evidence in two high-z SN Ia spectra of a double-absorption feature in Ca II λ3945, an event also observed, although infrequently, in low-redshift SN Ia spectra (6 out of 22 SNe Ia in our local sample). Moreover, echoing the recent studies of Dessart & Hillier in the context of Type II supernovae (SNe II), we see similar P Cygni line profiles in our large sample of SN Ia spectra. First, the magnitude of the velocity location at maximum profile absorption may underestimate that at the continuum photosphere, as observed, for example, in the optically thinner line S II λ5640. Second, we report for the first time the unambiguous and systematic intrinsic blueshift of peak emission of optical P Cygni line profiles in SN Ia spectra, by as much as 8000 km s^{-1}. All the high-z SNe Ia analyzed in this paper were discovered and followed up by the ESSENCE collaboration and are now publicly available.

Key words: cosmology: observations — line: formation — line: profiles — supernovae: general

Online material: color figures, machine-readable tables

[1] Based in part on observations obtained at the Cerro Tololo Inter-American Observatory, which is operated by the Association of Universities for Research in Astronomy (AURA), Inc., under cooperative agreement with the National Science Foundation (NSF); the European Southern Observatory, Chile (ESO program 170.A-0519); the Gemini Observatory, which is operated by AURA under a cooperative agreement with the NSF on behalf of the Gemini partnership (the NSF [United States], the Particle Physics and Astronomy Research Council [United Kingdom], the National Research Council [Canada], CONICYT [Chile], the Australian Research Council [Australia], CNPq [Brazil], and CONICET [Argentina]) (programs GN-2002B-Q-14, GN-2003B-Q-11, and GS-2003B-Q-11); the Magellan Telescopes at Las Campanas Observatory; the MMT Observatory, a joint facility of the Smithsonian Institution and the University of Arizona; and the F. L. Whipple Observatory, which is operated by the Smithsonian Astrophysical Observatory. Some of the data presented herein were obtained at the W. M. Keck Observatory, which is operated as a scientific partnership among the California Institute of Technology, the University of California, and the National Aeronautics and Space Administration. The Observatory was made possible by the generous financial support of the W. M. Keck Foundation.

[2] European Southern Observatory, Karl-Schwarzschild-Strasse 2, Garching D-85748, Germany; sblondin@eso.org, bleibund@eso.org, jspyromi@eso.org.

[3] Steward Observatory, University of Arizona, 933 North Cherry Avenue, Tucson, AZ 85721; luc@as.arizona.edu.

[4] Department of Physics and Astronomy, University of Oklahoma, Norman, OK 73019; branch@nhn.ou.edu.

[5] Department of Astronomy, University of Texas, Austin, TX 78681; pah@hej1.as.utexas.edu.

[6] Institute for Astronomy, University of Hawaii, 2680 Woodlawn Drive, Honolulu, HI 96822; barris@ifa.hawaii.edu, jt@ifa.hawaii.edu.

[7] National Optical Astronomy Observatory, 950 North Cherry Avenue, Tucson, AZ 85719-4933; matheson@noao.edu.

[8] Department of Astronomy, University of California, Berkeley, CA 94720-3411; rfoley@astro.berkeley.edu, chornock@astro.berkeley.edu, alex@astro.berkeley.edu, sjha@astro.berkeley.edu, weidong@astro.berkeley.edu.

[9] Stockholm Observatory, AlbaNova, SE-106 91 Stockholm, Sweden; jesper@astro.su.se.

[10] Harvard-Smithsonian Center for Astrophysics, 60 Garden Street, Cambridge, MA 02138; kirshner@cfa.harvard.edu, pchallis@cfa.harvard.edu, mhicken@cfa.harvard.edu, cstubbs@fas.harvard.edu, wmwood-vasey@cfa.harvard.edu.

[11] Departamento de Astronomía y Astrofísica, Pontificia Universidad Católica de Chile, Casilla 306, Santiago 22, Chile; aclocchi@astro.puc.cl.

[12] Cerro Tololo Inter-American Observatory, Casilla 603, La Serena, Chile; caguilera@ctio.noao.edu, arest@noao.edu, csmith@noao.edu, nsuntzeff@noao.edu.

[13] Department of Astronomy, University of Washington, Box 351580, Seattle, WA 98195-1580; becker@darkstar.astro.washington.edu, ricardo@astro.washington.edu, amiceli@astro.washington.edu.

[14] Research School of Astronomy and Astrophysics, Australian National University, Mount Stromlo and Siding Spring Observatories, Cotter Road, Weston Creek, ACT 2611, Australia; tamarad@mso.anu.edu.au, salvo@mso.anu.edu.au, brian@mso.anu.edu.au.

[15] Department of Physics, University of Notre Dame, 225 Nieuwland Science Hall, Notre Dame, IN 46556-5670; pgarnavi@nd.edu, kkrisciu@nd.edu.

[16] Department of Physics, Harvard University, 17 Oxford Street, Cambridge, MA 02138.

[17] Department of Physics, University of Washington, Box 351560, Seattle, WA 98195-1560; gm@u.washington.edu.

[18] Department of Astronomy, Ohio State University, 4055 McPherson Laboratory, 140 West 18th Avenue, Columbus, OH 43210; prieto@astronomy.ohio-state.edu.

[19] Space Telescope Science Institute, 3700 San Martin Drive, Baltimore, MD 21218; ariess@stsci.edu.

1. INTRODUCTION

Type Ia supernovae (SNe Ia) have been the subject of intense theoretical modeling and dedicated observational campaigns in recent years. The implications of relative luminosity distance measurements for low-redshift and high-redshift SNe Ia, namely, the requirement for an additional negative pressure term in Einstein's field equations ("dark energy"), are extraordinary for cosmologists and particle physicists alike (Riess et al. 1998; Perlmutter et al. 1999; see Filippenko [2004, 2005] for recent reviews). These results have not only been confirmed at moderate redshifts (Tonry et al. 2003; Knop et al. 2003; Barris et al. 2004) but also at higher ($z > 1$) redshifts, where the universal expansion is in a decelerating phase (Riess et al. 2004). Currently, two ongoing projects are aiming to measure the equation-of-state parameter of the dark energy: the ESSENCE (Equation of State: SupErNovae trace Cosmic Expansion; G. Miknaitis et al. 2006, in preparation; Krisciunas et al. 2005; Matheson et al. 2005) and SNLS (Supernova Legacy Survey; Pritchet 2005) projects.

A substantial motivation for precisely determining potential nonuniformity among high- and low-redshift SNe Ia is how those differences would impact cosmological models. For example, the use of SNe Ia as distance indicators requires an empirical relation, verified for nearby SNe Ia, between light-curve width and maximum luminosity (Phillips 1993). The extrapolation of such a relation to SNe Ia at higher redshifts might be inaccurate, possibly arising from distinct progenitor properties or yet unknown differences in the explosion mechanism (see Hillebrandt & Niemeyer [2000], Leibundgut [2001], and Höflich et al. [2003] for reviews).

Such evolutionary effects, however, would also need to explain the apparent brightening of SNe Ia at $z \gtrsim 1$ (Riess et al. 2004). Recently, Krisciunas et al. (2004a) noted the absence of a relation between luminosity and light-curve shape in the near-infrared (*JHK* bands), opening up exciting prospects for future high-z SN Ia observations in this (rest-frame) passband. In the meantime, it is worthwhile to look for potential differences between SNe Ia at different redshifts, based on their light-curve properties.

Spectroscopy is better suited than photometry to making quantitative comparisons between local and high-z SNe Ia. Large amounts of information are conveyed by spectra on the properties of the ejecta (chemical composition, velocity/density gradients, excitation level); subtle differences, blurred together in photometric measurements, will show up in the spectra. So far, comparisons of SNe Ia at different redshifts have only been qualitative in nature (Coil et al. 2000; Leibundgut & Sollerman 2001), although preliminary results of a quantitative analysis have been presented by Lidman (2004). The ESSENCE spectra published by Matheson et al. (2005) clearly show that a significant fraction of the high-z data are of sufficient quality for such comparisons, made possible through the public availability of many local SN Ia data via the SUSPECT database.[20] The high-z data, presented by Matheson et al. (2005), are now publicly available.[21]

The optical spectra of SNe Ia near maximum light are dominated by resonance lines of singly ionized, intermediate-mass elements, Doppler-broadened due to the large expansion velocities in SN Ia envelopes; see Filippenko (1997) for an observational review. Optically thick lines forming in such fast-expanding ejecta have a P Cygni profile shape, essentially characterized by absorption blueward of line center and peak emission at line center (Kirshner et al. 1973). Although these two components always appear qualitatively similar in P Cygni profiles associated with optically thick outflows, there are significant differences, which may become relevant if one seeks an accurate association with, e.g., the velocity at the photosphere—defined here as the outflow location where the inward integrated *continuum* optical depth is 2/3—of the SN ejecta (Kirshner & Kwan 1974) or, in another context, with the asymptotic velocity of a radiatively driven hot star wind (Prinja et al. 1990).

Recently, Dessart & Hillier (2005a, 2005b) performed detailed analyses of line-profile formation in SN II spectra, using hydrogen Balmer lines and Fe II λ5169 diagnostics. The origin of the possible underestimate of the photospheric velocity with the use of $v_{\rm abs}$ for optically thinner lines was identified by Branch (1977) but explained for the first time in Dessart & Hillier (2005b). Dessart & Hillier (2005a) also explained the origin of the significant blueshift of P Cygni profile emission compared to the rest wavelength of the corresponding line: for SN 1987A on 1987 February 24, this blueshift was on the order of 7000 km s^{-1}, equivalent to a very sizable 150 Å (see, e.g., Dessart & Hillier 2005a).

Both effects result from the fast-declining density distribution in SNe II, with $n \approx 10$ for a power law given by $\rho(r) = \rho_0(R_0/r)^n$, where r is the radius and R_0 and ρ_0 are some reference radius and density, respectively. Although the density drop-off in SNe Ia is estimated to be smaller (see, e.g., Höflich 1995), with $n \approx 7$, this is still large enough for the above two effects to occur. Such velocity shifts are not trivial; they represent key observables to constrain the density distribution and the sites of line formation (and interpret, for example, line-polarization measurements), the magnitude of disk-occultation and continuum optical-depth effects, and the ubiquitous but modulated influence of line overlap. The velocity locations corresponding to maximum absorption and peak emission are thus carriers of important information on the SN ejecta; they are, moreover, convenient and well-defined observables and can thus be used to objectively compare SNe Ia at different redshifts. The present paper is the result of such an investigation, using 229 spectra of local ($z < 0.05$) and 48 spectra of high-z ($0.16 < z < 0.64$) SNe Ia at phases between -2 weeks and +3 weeks from maximum light.

To minimize measurement biases, introduced primarily by the signal-to-noise ratio (S/N) obtained for the faint, high-redshift SNe Ia, we develop a spectral smoothing technique, which takes account of the expected large widths of observed SN Ia spectral features. We give a detailed account of our measurement technique and associated error model in § 2. The results of these measurements are presented in § 3, with individual discussion of $v_{\rm abs}$ and $v_{\rm peak}$ for Ca II λ3945, Si II λ6355, and S II $\lambda\lambda$5454, 5640. We discuss the wide range of $v_{\rm abs}$ values found for the different lines, the large magnitude of $v_{\rm peak}$ for the optically thinner lines S II $\lambda\lambda$5454, 5640, and the detection, for the first time, of double-absorption features in Ca II λ3945 in high-z SN Ia spectra. We provide insights into the nature of the above measurements by illustrating, following Dessart & Hillier (2005a, 2005b), some aspects of line and continuum formation in SN Ia spectra; namely, we explain the origin of the blueshift of peak emission and the relation of the absorption velocity to the photospheric and expansion velocities. In § 4 we present our conclusions.

2. MEASUREMENT TECHNIQUES

Any comparison between low-z and high-z SN Ia spectra suffers from the significantly degraded signal quality for the latter, due to the limited integration time available per spectrum when

[20] SUpernova SPECTrum Archive, http://nhn.ou.edu/~suspect.

[21] See http://www.noao.edu/noao/staff/matheson/spectra.html; the VLT spectra are also publicly available via the ESO archive, http://archive.eso.org/archive/public_datasets.html.

undertaking large SN Ia surveys (Matheson et al. 2005). To minimize this bias, we have developed a smoothing technique, presented in detail in § 2.1.

2.1. *Smoothing Supernova Spectra*

We apply a filter to both local and high-z SN Ia spectra to measure the absorption and emission-peak velocities in a consistent manner. This filter takes into account the wavelength-dependent nature of the noise in optical ground-based spectra and is based on the fact that SN spectral features are intrinsically broadened due to the large expansion velocity in the corresponding line-formation region. Assuming this broadening to have typical values of $\sim$1000–3000 km s^{-1}, one can write a "smoothing factor" $d\lambda/\lambda$ as (c is the speed of light in a vacuum)

$$\Delta v_{\rm line} \approx (0.003-0.01)c \quad \Longrightarrow \quad \frac{d\lambda}{\lambda} \approx 0.003-0.01. \quad (1)$$

For such a spectrum, a well-suited filter is a Gaussian of the same width, $\sigma_{\rm G}$. This assumes the S/N of the spectrum to be uniform over the whole wavelength range, which is clearly not the case for ground-based observations in which sky emission lines increase the noise in the red part of the spectrum. Thus, we instead adopt an inverse-variance-weighted Gaussian filter.

Let $\boldsymbol{F}_{\rm SN}$ and $\boldsymbol{F}_{\rm var}$ be the one-dimensional, flux-calibrated SN spectrum and its corresponding variance spectrum (usually the variance of the optimally extracted spectrum; see Horne 1986). Both spectra share the same wavelength axis, $\boldsymbol{\lambda}$. At each wavelength element λ_i, construct a Gaussian $\boldsymbol{G}_i$ of width

$$\sigma_{{\rm G},i} = \lambda_i \frac{d\lambda}{\lambda}. \quad (2)$$

We thus have

$$\boldsymbol{G}_i = \begin{pmatrix} G_{i,1} \\ G_{i,2} \\ \vdots \\ G_{i,N_l} \end{pmatrix} = \frac{1}{\sqrt{2\pi}} \exp\left[-\frac{1}{\sigma_{{\rm G},i}} \begin{pmatrix} \lambda_1 - \lambda_i \\ \lambda_2 - \lambda_i \\ \vdots \\ \lambda_{N_l} - \lambda_i \end{pmatrix} \right]^2, \quad (3)$$

where N_l is the number of wavelength elements of a subset of $\boldsymbol{\lambda}$, centered on λ_i. The inverse-variance-weighted Gaussian is then

$$\boldsymbol{W}_i = \begin{pmatrix} W_{i,1} \\ W_{i,2} \\ \vdots \\ W_{i,N_l} \end{pmatrix} = \begin{pmatrix} G_{i,1}/F_{{\rm var},1} \\ G_{i,2}/F_{{\rm var},2} \\ \vdots \\ G_{i,N_l}/F_{{\rm var},N_l} \end{pmatrix}, \quad (4)$$

and the corresponding smoothed flux at λ_i is therefore

$$F_{{\rm TS},i} = \frac{\sum_j W_{i,j} F_{{\rm SN},j}}{\sum_j W_{i,j}}. \quad (5)$$

By repeating this process for each wavelength element λ_i, we obtain the smoothed SN spectrum $\boldsymbol{F}_{\rm TS}$.

We show the result of applying this spectral smoothing algorithm with $d\lambda/\lambda = 0.005$ in Figure 1. The upper spectrum is that of SN 2003jy ($z = 0.339$), plotted as a function of rest wavelength. The spectrum just below is the smoothed version, showing how most of the high-frequency noise has been removed, while the lower frequency SN spectral features have been preserved. In this paper we use the same smoothing factor, $d\lambda/\lambda = 0.005$, in applying this smoothing technique to both the local and high-z SN Ia spectra.

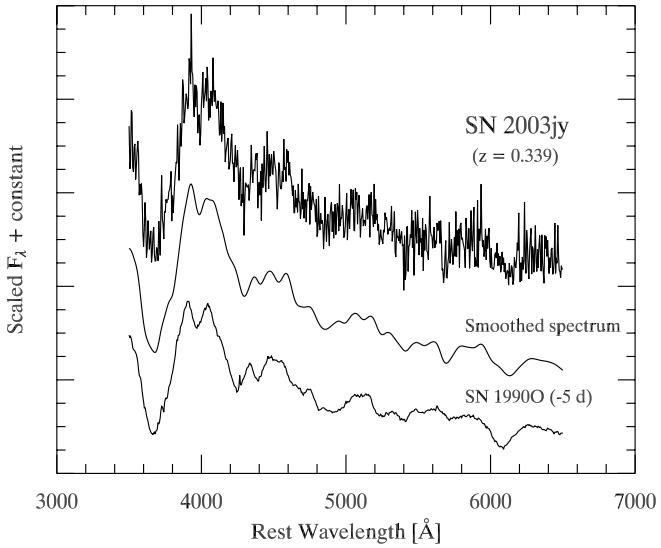

FIG. 1.—*Top to bottom*: High-z SN Ia spectrum (SN 2003jy; $z = 0.339$), its smoothed version (with $d\lambda/\lambda = 0.005$), and a local zero-redshift template (SN 1990O at -5 days), plotted for comparison with the smoothed spectrum.

We show examples of smoothed spectra of several local SNe Ia at different phases (and with different S/N) in Figure 2, where we concentrate on the Si II λ6355 feature plotted in velocity space (assuming $\lambda_0 = 6355$ Å and using the relativistic Doppler formula). We also show (*arrows*) the location of maximum absorption and the emission peak, measured with our smoothing technique and corresponding to $v_{\rm abs}$ and $v_{\rm peak}$. We see that line profiles in SNe Ia come in many shapes and sizes, from the well-defined absorption trough of SN 1992A at -5 days to the flat-bottomed one of SN 1990N at -13 days, which extends $\gtrsim$5000 km s^{-1} (perhaps due to contamination from C II λ6580; see Fisher et al. 1997; Mazzali 2001). The emission-peak region is often less well defined than the absorption trough (Jeffery & Branch 1990) and is more affected by contamination by emission from iron-group elements at late phases ($\gtrsim$2 weeks past maximum brightness). Our spectral smoothing technique does a fine job of reproducing the broad features in SN Ia spectra, both for low-S/N spectra and for contaminated line profiles.

For some spectra we do not have a corresponding variance spectrum at our disposal, either because these variance spectra are not archived in the spectral databases (this is the case for many local SN Ia spectra) or because the pipeline used to reduce the spectra did not generate the variance spectra (as was the case for spectra taken with the Keck Low Resolution Imaging Spectrometer at the time of data reduction). For these spectra we use a fiducial sky spectrum taken with the same telescope-instrument combination in place of a variance spectrum. This is adequate, since our smoothing technique relies on the relative variance only, and we expect sky emission to be the dominant source of noise in our optical ground-based spectra.

We then spline interpolate the smoothed spectrum $\boldsymbol{F}_{\rm TS}$ onto a 0.1 Å resolution grid and determine the wavelengths of maximum absorption ($\lambda_{\rm abs}$) and emission peak ($\lambda_{\rm peak}$). The absorption

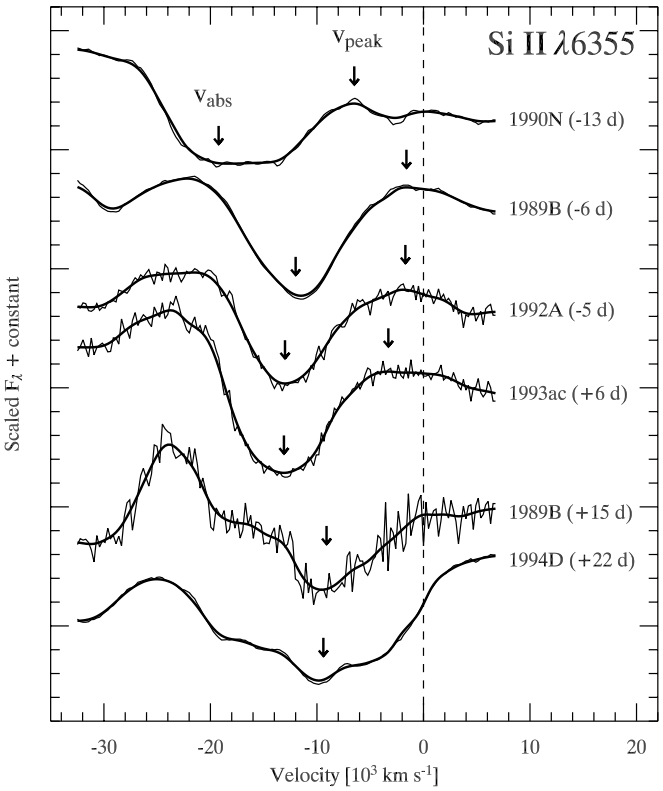

FIG. 2.—P Cygni profiles of Si II λ6355 in local SNe Ia. Overplotted on the spectra are their smoothed versions (thick black lines; see § 2.1). The arrows indicate the measured maximum absorption and emission peak, used to determine $v_{\rm abs}$ and $v_{\rm peak}$. Contamination of the sides of the Si II absorption profile by strengthening emission/absorption from iron-group elements is apparent at late phases (≳2 weeks) and prevents us from measuring the emission-peak velocity.

and emission-peak velocities are then calculated using the relativistic Doppler formula,

$$v_{\rm Doppler,\,rel} = c\left\{\frac{[(\Delta\lambda/\lambda_0)+1]^2-1}{[(\Delta\lambda/\lambda_0)+1]^2+1}\right\}, \qquad (6)$$

where $\Delta\lambda = \lambda_{\rm abs} - \lambda_0$ and $\lambda_{\rm peak} - \lambda_0$ when inferring $v_{\rm abs}$ and $v_{\rm peak}$, respectively, and λ_0 is the rest-frame wavelength of the corresponding transition.

This approach has the advantage over using a Gaussian fit to the overall absorption/emission profiles, since it makes no assumption about their shape (in particular, whether the absorption/emission profiles are symmetric). Moreover, fitting a function to the whole ∼100–200 Å wide profiles would enhance the impact of line overlap on the fit. In Figure 3 we show velocity residuals as a function of S/N when using a Gaussian fit to the absorption profile and when spline interpolating a spectrum smoothed using our algorithm. Here the "noise" is defined as the rms deviation between the input spectrum $\boldsymbol{F}_{\rm SN}$ and the filtered spectrum $\boldsymbol{F}_{\rm TS}$, with $d\lambda/\lambda = 0.005$:

$$\mathrm{S/N} = \frac{\overline{|\boldsymbol{F}_{\rm SN}|}}{\sqrt{(1/N_\lambda)\sum_{j=1}^{N_\lambda}(|F_{{\rm SN},j}| - |F_{{\rm TS},j}|)^2}}, \qquad (7)$$

where N_λ is the number of elements in $\boldsymbol{\lambda}$. We find this to be an accurate description of the actual mean S/N, which then enables us to evaluate the mean S/N of spectra for which we do not have the corresponding variance spectrum.

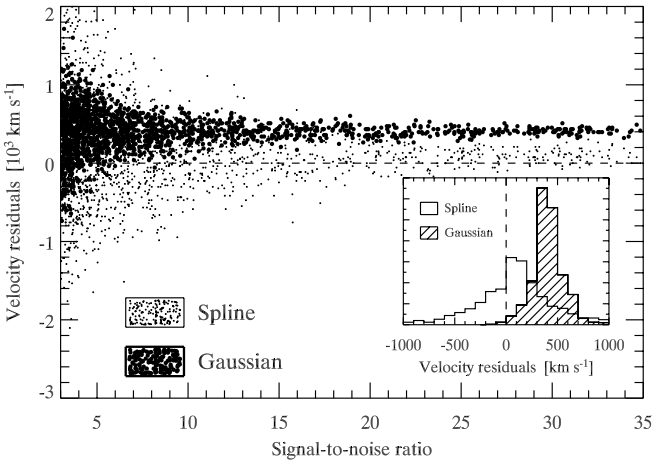

FIG. 3.—Velocity residuals when fitting the minimum of the P Cygni profile of Si II λ6355 in 1989B at −6 days with a Gaussian (*large dots*) or when determining the minimum from a spline interpolation of an inverse-variance-weighted Gaussian spectrum (*small dots*). The original S/N of the spectrum is ∼70. Each of the dots corresponds to the original spectrum, to which we have added random Poisson noise weighted by a fiducial sky spectrum. The inset shows the distribution of velocity residuals for both the spline (*open histogram*) and Gaussian (*hatched histogram*) techniques.

Each of the points in Figure 3 corresponds to a fit to the absorption profile of Si II λ6355 in SN 1989B at −6 days (S/N ≈ 70 in that spectral region), for which we have added increasing random Poisson noise weighted by a fiducial sky spectrum, to reproduce S/Ns in the range 2–40. In this case, we have a systematic error of approximately +400 km s^{-1} when using a Gaussian, while this uncertainty drops to ≲100 km s^{-1} for the spline-interpolation method. The latter method is more sensitive to the S/N; namely, the drop in precision with decreasing S/N is more significant for the spline ($\sigma_{\rm spline} \approx 320$ km s^{-1}) than for the Gaussian ($\sigma_{\rm G} \approx 130$ km s^{-1}). We use such simulations to evaluate the error due to a spectrum's S/N on our inferred values of $v_{\rm abs}$ and $v_{\rm peak}$ (see § 2.2). All the measurements in this paper make use of the spline-interpolation method.

2.2. *Error Budget*

In this section we give a detailed account of the various sources of systematic error. We give estimates of these errors in Table 1. The elaboration of an error model is an important part of the comparison of $v_{\rm abs}$ and $v_{\rm peak}$ among local SNe Ia and between the local and high-z SNe Ia. Several authors presenting measurements of $v_{\rm abs}$ in local SNe Ia either do not give their error models (Benetti et al. 2005) or do not report errors at all (Patat et al. 1996).

Note that we do not include errors related to line blending, as this would require detailed modeling of every individual spectrum. We discuss the issue of line blending when presenting our results in § 3.

2.2.1. *Errors Related to the Measurement*

The smoothing and spline-interpolation technique we use to measure the absorption and emission-peak velocities minimizes the impact of inherently asymmetric profiles. However, in some cases we are unable to rely entirely on this method. This occurs when (1) the profile is highly skewed over a wavelength scale $\Delta\lambda/\lambda < d\lambda/\lambda$ ($d\lambda/\lambda = 0.005$ here); (2) the feature is too weak, yet a minimum is clearly identifiable; (3) the absorption profile has a flat minimum (e.g., Si II λ6355 in SN 1990N at early phases; Fig. 2); and (4) there is a sharp feature that affects the smoothing technique (galaxy line, cosmic ray, noise spike). For cases 1 and

TABLE 1
Measurement Errors

Error Source	Error Size (km s^{-1})
Errors Related to SN Ia Spectral Properties	
Line blending/contamination	Not included
Contamination from host galaxy	Not included
Errors Related to the Measurement	
Skewed profile	$\sim$1000
S/N	$\sim$200, 500, 700, and 1200 for S/N $\approx$ 20, 10, 5, and 2 per 5 Å bin
Other Errors	
Redshift uncertainty	$\sim$200 and 3000 for galaxy and SN redshift
Reddening uncertainty $\sigma_{E(B-V)}$	$\lesssim$100 for $\sigma_{E(B-V)} \lesssim 0.5$ mag
Use of classical Doppler formula	$\sim$200, 400, and 600 for $v \approx$ 10, 15, and 20 $\times$ 10^3 km s^{-1}

2 we resort to a smaller smoothing factor ($0.001 \leq d\lambda/\lambda \leq 0.003$). For case 3 we report the velocity corresponding to the blue edge (i.e., the optically thinner part) of the absorption profile and associate a lower error bar corresponding to the velocity difference between the blue and red edges of the profile. For case 4 we simply use a linear interpolation over the sharp feature when its width is less than $(d\lambda/\lambda)\lambda_{\rm abs}$ (for $v_{\rm abs}$ measurements) or $(d\lambda/\lambda)\lambda_{\rm peak}$ (for $v_{\rm peak}$ measurements).

The S/N of the input spectrum will limit the accuracy of the measurement. For every local SN Ia spectrum in our database, we progressively degrade the S/N of the spectrum by adding random Poisson noise weighted by a fiducial sky spectrum (see § 2.1) and construct plots of velocity residuals versus S/N (as in Fig. 3) for each of the four spectral features studied here. Most of the local SN Ia spectra used in this study have S/N > 10 (per 5 Å bin), and the associated error is $\lesssim$500 km s^{-1} (Table 1), whereas for many of the high-z spectra, the error due to poor S/N can be $>$1000 km s^{-1}.

2.2.2. *Further Errors*

Further errors affecting measurements of $v_{\rm abs}$ and $v_{\rm peak}$ include the following:

Redshift of parent galaxy.—All the SN spectra have been corrected for the heliocentric velocity of their host galaxy, $z_{\rm gal}$. This measurement is affected not only by the galaxy's internal velocity dispersion ($\sim$200 and 100 km s^{-1} for early- and late-type galaxies, respectively; McElroy 1995) but also by the position of the SN within the galaxy. An illustration of this is SN 1994D in NGC 4526, for which the NASA/IPAC Extragalactic Database (NED) gives $cz = +448$ km s^{-1} but King et al. (1995) measure $cz = +880$ km s^{-1}, at the SN position. We have therefore added a $\sigma_{cz,\rm gal} \approx 200$ km s^{-1} error in quadrature to the total error to account for this effect. Note that for some of the high-z SNe Ia, the redshift has been determined via cross-correlation with local SN Ia spectral templates, with a typical error $\sigma_{z,\rm SN} \approx 0.01 \equiv 3000$ km s^{-1} (Matheson et al. 2005). Thus, for these high-z SNe, the major source of error is due to redshift. Note that such an error leads to a global shift in velocity and is different in nature from effects such as line overlap, which are difficult to assess and vary from line to line.

Reddening.—All the local and high-z SN Ia spectra have been corrected for both host-galaxy and Galactic (Schlegel et al. 1998) reddening. For the local SNe Ia, we use the host-galaxy reddenings of Phillips et al. (1999) (see Table 2). For the high-z SNe Ia, we use the reddening values derived from fitting the light curves using the algorithm of Prieto et al. (2006). An error in the reddening correction applied to a spectrum can affect the overall continuum slope and in turn bias $v_{\rm abs}$ to higher (lower) values, if the reddening is underestimated (overestimated). We have run a simulation to evaluate the errors associated with reddening misestimates. They are $\lesssim$50 km s^{-1} for $\sigma_{E(B-V)} \lesssim 0.3$ mag. Since the reddening is typically known down to $\sim$0.1 mag in local and high-z SNe Ia (see Tables 2 and 3), we ignore this error.

Host-galaxy contamination.—We do not include errors related to contamination of SN Ia spectra by host-galaxy light. The S/N of most local SN Ia spectra is such that the line shapes are expected to be little affected by host-galaxy contamination. For the high-z data, we cannot make this assumption, nor do we have a reliable way of evaluating the amount of galaxy light present in our spectra, and we ignore this error. All the Very Large Telescope (VLT) spectra analyzed here and presented by Matheson et al. (2005) were extracted using a two-dimensional deconvolution technique employing the Richardson-Lucy restoration method, minimizing the contamination from the host galaxy (Blondin et al. 2005). However, we see no systematic effect between the VLT spectra and those from other telescopes.

We further assume the wavelength calibration to be accurate to within $\pm$0.5 Å, which corresponds to errors $<$50 km s^{-1} (not included in the error budget).

We note that, since absorption velocities in SN Ia ejecta can reach $\sim$30,000 km s^{-1} ($0.1c$), relativistic corrections to the classical Doppler formula become noticeable ($\sim$1500 km s^{-1}). Different authors may or may not apply the relativistic Doppler formula in their determination of absorption velocities, and systematic differences can result from a blind comparison of different measurements. All the velocities calculated here make use of the relativistic Doppler formula; this is not strictly consistent when comparisons are made with model atmosphere computations that do not explicitly take into account the relativistic terms in the radiative transfer equation.

An error in the SN phase is of a different nature, as it is not a direct error on a velocity measurement but rather an indirect one affecting the correlation of $v_{\rm abs}$ and $v_{\rm peak}$ measurements with SN phase. The typical error in the time of rest-frame B-band maximum is $\lesssim$1 day (Table 2). This error will, of course, directly propagate as an error in the phase of the SN spectrum. For the local SNe Ia, we use an updated version of the multicolor light-curve shape (MLCS) method of Riess et al. (1996), MLCS2k2 (Jha

TABLE 2

LOCAL SN Ia DATA

SN IAU Name (1)	Host Galaxy (2)	cz (3)	$E(B-V)$ (4)	M_B (5)	Δm_{15} (6)	$\mathrm{HJD_{max}}$ (7)	Phases (8)	References (9)
1981B	NGC 4536	1808	0.11 (0.03)	−19.616 (0.038)	1.10 (0.07)	44,670.95 (0.73)	+0, +6, +17, +20, +24	1
1986G	NGC 5128	547	0.50 (0.05)	−18.273 (0.113)	1.73 (0.07)	46,561.36 (0.24)	−[5-1], +[0-3], +5	2, 3
1989B	NGC 3627 (M66)	727	0.34 (0.04)	−19.537 (0.064)	1.31 (0.07)	47,564.32 (0.59)	−6, +0, +4, +6, +[8-9], +10, +[12-15], +18	4, 5, 6, 7
1990N	NGC 4639	1010	0.09 (0.03)	−19.704 (0.022)	1.07 (0.05)	48,081.89 (0.17)	−[14-13], −[8-6], +5, +8, +[17-18]	8
1990O	MCG +03-44-3	9193	0.02 (0.03)	−19.657 (0.037)	0.96 (0.10)	48,076.13 (1.02)	−[7-5], +0, +[20-21]	9
1991T	NGC 4527	1736	0.14 (0.05)	−19.694 (0.015)	0.94 (0.05)	48,374.03 (0.14)	+[8-11], +[14-17], +26	10, 11, 12
1991bg	NGC 4374 (M84)	1060	0.03 (0.05)	−17.604 (0.098)	1.93 (0.10)	48,603.12 (0.31)	+[1-3], +[15-16], +19, +26	13, 14, 15
1992A	NGC 1380	1877	0.00 (0.02)	−19.148 (0.062)	1.47 (0.05)	48,640.63 (0.19)	−5, +0, +3, +[5-7], +9, +12, +16, +17	16
1993ac	Anon.	14791[a]	0.12 (0.04)	−19.599 (0.071)	1.19 (0.10)	49,269.70 (1.19)	+6	...
1994D	NGC 4526	448	0.00 (0.02)	−19.452 (0.030)	1.32 (0.05)	49,432.47 (0.10)	−[11-2], +[2-3], +[10-13], +15, +17, +19, +22, +24, +29	17, 18, 19
1994M	NGC 4493	6943	0.08 (0.03)	−19.345 (0.076)	1.44 (0.10)	49,473.61 (0.90)	+[3-5], +8, +13	9
1994S	NGC 4495	4550	0.00 (0.03)	−19.617 (0.046)	1.10 (0.10)	49,518.28 (0.50)	+0, +2, +5	9
1994T	Anon.	10399[a]	0.09 (0.04)	−18.778 (0.148)	1.39 (0.10)	49,514.54 (0.52)	+3, +5, +8	...
1994ae	NGC 3370	1279	0.12 (0.03)	−19.679 (0.019)	0.86 (0.05)	49,684.65 (0.15)	−1, +[0-5], +[8-10], +29	...
1995D	NGC 2962	1966	0.04 (0.02)	−19.676 (0.021)	0.99 (0.05)	49,768.60 (0.44)	+[3-5], +7, +9, +11, +[14-15]	20
1995E	NGC 2441	3470	0.74 (0.03)	−19.558 (0.041)	1.06 (0.05)	49,774.67 (0.54)	−[3-1], +1, +8	...
1995al	NGC 3021	1541	0.15 (0.03)	−19.722 (0.015)	0.83 (0.05)	50,028.95 (0.44)	+17, +26	...
1995bd	UGC 3151	4377	0.15 (0.06)	−19.703 (0.024)	0.84 (0.05)	50,086.31 (0.24)	+12, +16, +21	...
1996C	MCG +08-25-47	8094	0.09 (0.03)	−19.630 (0.033)	0.97 (0.10)	50,128.42 (0.90)	+8	...
1996X	NGC 5061	2065	0.01 (0.02)	−19.490 (0.038)	1.25 (0.05)	50,190.85 (0.33)	−[3-1], +[0-3], +[7-9], +13, +22, +24	21, 22
1996Z	NGC 2935	2271	0.33 (0.04)	−19.482 (0.167)	1.22 (0.10)	50,215.25 (1.45)	+6	...
1997br	ESO 576-40	2080	0.24 (0.10)[b]	−19.731 (0.013)	1.00 (0.15)[b]	50,559.26 (0.23)	−[9-6], −4, +8, +18, +24	23
1997cn	NGC 5490	4855	0.00 (...)[c]	−17.656 (0.095)	1.86 (...)[c]	50,586.64 (0.78)	+4	24
1998aq	NGC 5584	1638	0.08 (...)[d]	−19.604 (0.023)	1.15 (0.05)[e]	50,930.80 (0.13)	−[9-8], +[0-7]	25, 26
1998bu	NGC 3368 (M96)	897	0.33 (0.03)	−19.572 (0.026)	1.01 (0.05)	50,952.40 (0.23)	−[3-1], +[9-14], +[28-30]	27, 28

TABLE 2—*Continued*

SN IAU Name (1)	Host Galaxy (2)	cz (3)	$E(B-V)$ (4)	M_B (5)	Δm_{15} (6)	$\mathrm{HJD}_{\max}$ (7)	Phases (8)	References (9)
1999aa	NGC 2565	4330	0.00 (...)[f]	−19.726 (0.012)	0.75 (0.02)[f]	51,231.97 (0.15)	−[9-1], +1, +[15-18], +[27, 30]	29, 30
1999by	NGC 2841	638	0.00 (...)[g]	−17.719 (0.061)	1.90 (0.05)[g]	51,309.50 (0.14)	−[5-3], +8, +11, +25, +29	31, 32, 33
1999ee	IC 5179	3422	0.28 (0.04)[h]	−19.688 (0.015)	0.94 (0.06)[h]	51,469.29 (0.14)	−9, −7, −2, +0, +2, +7, +11, +16, +19, +22, +27	34, 35
2000cx	NGC 524	2379	0.00 (...)[i]	−19.484 (0.021)	0.93 (0.04)[i]	51,752.40 (0.13)	−[2-1], +[0-1], +6, +7(2), +9, +11, +14, +19, +22	36
2002bo	NGC 3190	1271	0.43 (0.10)[j]	−19.595 (0.027)	1.13 (0.05)[j]	52,356.89 (0.14)	−11, −[9-8], −[6-5], −[4-1], +0, +6, +29	37

NOTES.—Col. (1): IAU designation. Col. (2): Name of SN host galaxy; Anon. (Anonymous) means the galaxy has no official designation. Col. (3): Heliocentric radial velocity of the host galaxy ($\mathrm{km\ s^{-1}}$) as quoted in the NED; we assume an error of 300 $\mathrm{km\ s^{-1}}$ in the galaxy redshift. Col. (4): Average host-galaxy reddening (mag) as quoted in Table 2, col. (7) of Phillips et al. (1999). Col. (5): Absolute B-band magnitude at maximum, derived from an MLCS2k2 fit to the rest-frame B-band light curves (Jha 2002; Jha et al. 2006). Col. (6): Decline in magnitudes in the rest-frame B band between maximum and +15 days, as quoted in Table 2, col. (2) of Phillips et al. (1999). Col. (7): Actual Heliocentric Julian Date −2,440,000 of B-band maximum; derived from an MLCS2k2 fit to the rest-frame B-band light curves. The 1 σ uncertainties are given in parentheses. Col. (8): Rest-frame phase in days from B-band maximum, rounded to closest whole day; adjacent phases are listed in brackets. A "(2)" indicates that two spectra correspond to the same rounded phase. Col. (9): References to refereed articles presenting optical spectroscopic data in the range $-15 \leq$ phase $\leq +30$ (days from B-band maximum), as found on the NASA Astrophysics Data System server; ellipses indicate that no references were found for a given SN. Table 2 is also available in machine-readable form in the electronic edition of the *Astronomical Journal*.

[a] From Table 3 of Riess et al. (1999a).

[b] From Li et al. (1999); the host galaxy $E(B-V)$ was determined from the total $E(B-V)$ quoted in Li et al. (1999) and a Galactic reddening of 0.11 mag, as derived using the dust infrared emission maps of Schlegel et al. (1998).

[c] From Turatto et al. (1998).

[d] From Saha et al. (2001). Note that this value assumes that the SN experiences the same reddening as the Cepheids in NGC 5584; see Saha et al. (2001) for a thorough discussion of this issue.

[e] From Riess et al. (1999b).

[f] From Krisciunas et al. (2000).

[g] From Garnavich et al. (2004); see this same paper for a long discussion on the low/null reddening in the host galaxy.

[h] From Stritzinger et al. (2002).

[i] From Li et al. (2001b).

[j] From Benetti et al. (2004); consult this paper and Krisciunas et al. (2004b) for an extensive discussion on the abnormally high $E(B-V)$ value obtained for SN 2002bo.

REFERENCES.—(1) Branch et al. 1983; (2) Frogel et al. 1987; (3) Phillips et al. 1987; (4) Bolte et al. 1989; (5) Barbon et al. 1990; (6) Wells et al. 1994; (7) Wells & Lee 1995 (erratum on Wells et al. 1994); (8) Leibundgut et al. 1991; (9) Gómez et al. 1996; (10) Filippenko et al. 1992a; (11) Ruiz-Lapuente et al. 1992; (12) Phillips et al. 1992; (13) Filippenko et al. 1992b; (14) Leibundgut et al. 1993; (15) Turatto et al. 1996; (16) Kirshner et al. 1993; (17) Höflich 1995; (18) Patat et al. 1996; (19) Meikle et al. 1996; (20) Sadakane et al. 1996; (21) Wang et al. 1997; (22) Salvo et al. 2001; (23) Li et al. 1999; (24) Turatto et al. 1998; (25) Vinkó et al. 1999; (26) Branch et al. 2003; (27) Jha et al. 1999; (28) Hernandez et al. 2000; (29) Li et al. 2001a; (30) Garavini et al. 2004; (31) Vinkó et al. 2001; (32) Howell et al. 2001; (33) Garnavich et al. 2004; (34) Hamuy et al. 2002a; (35) Hamuy et al. 2002b (erratum on Hamuy et al. 2002a); (36) Li et al. 2001b; (37) Benetti et al. 2004.

TABLE 3
HIGH-z SN Ia DATA

IAU Name	z[a]	$E(B-V)$[b]	$\Delta m_{15}(B)$[b]	$\mathrm{MJD_{max}}$[b]	Phases[c]
2002iy	0.587	0.01 (0.03)	0.93 (0.10)	52,592.75 (1.34)	+14
2002iz	0.428	0.14 (0.08)	1.17 (0.05)	52,587.80 (1.56)	−1, +19
2002ja	0.33	0.19 (0.08)	0.94 (0.09)	52,585.42 (1.97)	+2
2002jb	0.25	0.12 (0.10)	1.10 (0.03)	52,596.01 (0.67)	−7
2002jc	0.52	0.00 (0.02)	1.47 (0.04)	52,596.27 (0.52)	−6, +11
2002jd	0.32	0.00 (0.05)	0.84 (0.04)	52,593.29 (0.56)	−3, +16, +18
2002jq	0.49	0.06 (0.11)	1.48 (0.07)	52,603.47 (0.02)	+6
2002js	0.54	0.00 (0.03)	1.03 (0.07)	52,600.21 (1.19)	+7
2002jt	0.56	0.00 (0.07)	0.83 (0.01)	52,615.42 (1.34)	+3
2002jw	0.357	0.08 (0.05)	1.00 (0.08)	52,618.35 (0.76)	−2, +19
2003ji	0.21	0.00 (0.04)	0.84 (0.05)	52,921.14 (1.79)	+19
2003jj	0.583	0.25 (0.10)	0.84 (0.11)	52,946.83 (1.33)	−2
2003jl	0.429	0.15 (0.05)	0.92 (0.04)	52,931.72 (0.66)	+8
2003jm	0.522	0.05 (0.06)	0.84 (0.08)	52,933.97 (1.72)	+5
2003jo	0.524	0.00 (0.07)	0.84 (0.13)	52,935.81 (1.81)	+3
2003jq	0.16	0.30 (0.03)	0.83 (0.01)	52,935.25 (0.36)	+1
2003jr	0.340	0.18 (0.05)	0.83 (0.05)	52,920.76 (1.44)	+17
2003js	0.363	0.00 (0.01)	0.99 (0.03)	52,948.38 (0.40)	−5, +13
2003jt	0.45	0.12 (0.05)	0.83 (0.08)	52,936.84 (1.03)	+3
2003ju	0.20	0.06 (0.06)	1.29 (0.01)	52,948.44 (0.37)	−8, +18
2003jv	0.405	0.14 (0.07)	0.83 (0.10)	52,942.48 (1.01)	−2
2003jw	0.296	0.08 (0.10)	1.69 (0.01)	52,949.85 (0.48)	−6
2003jy	0.339	0.03 (0.04)	1.05 (0.04)	52,956.13 (0.53)	−10
2003kk	0.164	0.20 (0.05)	1.02 (0.03)	52,966.29 (0.39)	−4
2003kl	0.335	0.23 (0.11)	1.47 (0.08)	52,965.52 (1.46)	−3, +0
2003km	0.47	0.02 (0.03)	0.94 (0.04)	52,981.10 (0.46)	−12, −11
2003kn	0.244	0.15 (0.07)	1.47 (0.03)	52,974.01 (0.46)	−7
2003ko	0.360	0.20 (0.05)	1.21 (0.06)	52,968.25 (0.88)	−2
2003kp	0.64	0.02 (0.05)	1.29 (0.05)	52,963.14 (1.48)	+1
2003kq	0.61	0.09 (0.05)	0.88 (0.07)	52,969.64 (1.31)	−3
2003kr	0.427	0.09 (0.03)	1.17 (0.05)	52,976.71 (0.48)	−8
2003kt	0.61	0.02 (0.05)	1.23 (0.07)	52,959.82 (1.75)	+4
2003le	0.56	0.07 (0.08)	0.83 (0.02)	52,995.50 (1.56)	−1
2003lf	0.41	0.09 (0.04)	1.40 (0.07)	52,990.69 (0.57)	+2, +3
2003li	0.544	0.05 (0.05)	1.06 (0.04)	52,984.95 (1.23)	+5
2003lj	0.417	0.27 (0.09)	1.11 (0.07)	52,989.60 (1.60)	+3
2003lm	0.408	0.11 (0.05)	1.47 (0.05)	52,992.14 (0.91)	+2
2003ln	0.63	0.02 (0.04)	0.85 (0.18)	52,987.80 (1.23)	+4

NOTE.—Table 3 is also available in machine-readable form in the electronic edition of the *Astronomical Journal*.

[a] For redshifts determined from narrow lines in the host galaxy (quoted with three decimal places), we assume an error of ∼0.001; for those determined via cross-correlations with local SN Ia spectral templates (Matheson et al. 2005), we assume an error of 0.01.

[b] Light-curve parameters (and 1 σ errors) output by the fitting routine of Prieto et al. (2006); $E(B-V)$ values correspond to host-galaxy extinction only.

[c] Rest-frame phase in days from rest-frame B-band maximum, rounded to closest whole day.

2002; Jha et al. 2006), to determine the time of B-band maximum. We could use the MLCS2k2 1 σ error on $\mathrm{HJD_{max}}$ as the 1 σ error on the SN phase, but the MLCS2k2 templates are sampled only once per day, introducing sampling errors on the order of ∼0.5 day. For the local SNe Ia we add a fiducial ±0.5 day error in quadrature to the MLCS2k2 error in $\mathrm{HJD_{max}}$, while for the high-z SNe Ia we use the 1 σ error output by the light-curve fitting routine of Prieto et al. (2006).

3. RESULTS

In this section, using the above method, we present absorption (§ 3.1) and emission-peak (§ 3.2) velocity measurements for the Ca II λ3945, Si II λ6355, and S II $\lambda\lambda$5454, 5640 line profiles (Table 4). These lines do not have the same observed profile shape, presumably because they form differently, and have the potential to reveal distinct aspects of the SN outflow. Note that here these measurements are sometimes compared with the velocity at the photosphere; let us stress again that throughout this paper, we refer to the photosphere as the outflow location where the inward integrated *continuum* optical depth is 2/3; no account is made of line opacity in this definition.

Our sample comprises 30 local SNe Ia with phases between −14 and +30 days from B-band maximum (Table 2) and 37 high-z ($0.16 < z < 0.64$) SNe Ia with (rest-frame) phases between −12 and +19 days from (rest-frame) B-band maximum (Table 3; Matheson et al. 2005). We thus performed measurements for a total of 229 local and 48 high-z spectra. Emission-peak velocity measurements, more affected by line contamination (see Jeffery & Branch 1990), are only quoted for 178 local and 39 high-z spectra. In Tables 5–8 we present the relativistic Doppler velocities v_{abs} and v_{peak} corresponding to the above four line diagnostics, using for each the rest-frame wavelength given in Table 4. For the doublet lines of Ca II and Si II this corresponds to the gf-weighted mean wavelength, where g and f are

TABLE 4
CHARACTERISTIC WAVELENGTHS OF ATOMIC TRANSITIONS

Ion	Multiplet Designation	λ (Å)	log (gf)	λ_{gf} (Å)	$\lambda_{\rm used}$[a] (Å)
Ca II	$4s\ ^2S$–$4p\ ^2P^0$	3933.66, 3968.47	0.134, −0.166	3945.28	3945
S II[b]	$4s\ ^4P$–$4p\ ^4D^0$	5432.80, 5453.86	0.311, 0.557	5442.69	5454
S II[c]	$3d\ ^4F$–$4p\ ^4D^0$, $4s\ ^2P$–$4p\ ^2D^0$	5606.15, 5639.98	0.156, 0.330	5638.12	5640
Si II	$4s\ ^2S$–$4p\ ^2P^0$	6347.11, 6371.37	0.297, −0.003	6355.21	6355

NOTE.—From Kurucz & Bell (1995).
[a] Assumed rest-frame wavelength for the transition of the given ion; for Ca II and Si II this is simply the gf-weighted mean wavelength of the two strongest transitions, while for S II this is the wavelength corresponding to the strongest transition.
[b] There are five transitions corresponding to S II in the range 5400 Å $< \lambda <$ 5500 Å; we list the two corresponding to the largest gf-values. Note that the value for λ_{gf} corresponds to the gf-weighted mean of these five transitions.
[c] There are eight transitions corresponding to S II in the range 5600 Å $< \lambda <$ 5700 Å; we list the two corresponding to the largest gf-values. Note that the value for λ_{gf} corresponds to the gf-weighted mean of these eight transitions.

the statistical weight and oscillator strength of the transition, respectively. For the two S II features we instead use the wavelength of the highest log (gf) transition, due to the large number of transitions involved (see § 3.1.1).

To facilitate the visual inspection of figures, we show the temporal evolution of $v_{\rm abs}$ (Figs. 4, 6, and 7) and $v_{\rm peak}$ (Figs. 9–12) for all spectra by grouping data points according to the decline-rate parameter $\Delta m_{15}(B)$ (the decline in B-band magnitudes between maximum [+0 days] and +15 days; Phillips 1993; Phillips et al. 1999) of the corresponding SN Ia. Following this selection criterion, our sample of local (high-z) SNe Ia has 10 (17) objects with $\Delta m_{15}(B) < 1.0$, 17 (20) with $1.0 \leq \Delta m_{15}(B) \leq 1.7$, and 3 (0) with $\Delta m_{15}(B) > 1.7$; the lack of $\Delta m_{15}(B) > 1.7$ SNe Ia in our high-z sample could be due to a selection effect (G. Miknaitis et al. 2006, in preparation; Krisciunas et al. 2005). Note that when computing the decline rate $\Delta m_{15}(B)$ of high-z SNe Ia, time dilation is accounted for by scaling the time axis by a factor $(1 + z)^{-1}$ (Leibundgut et al. 1996; Goldhaber et al. 2001).

3.1. *Absorption Velocities*

All *spectroscopic* velocity measurements reported in this paper are negative and thus correspond to blueshifts; to avoid any confusion, we apply the standard rules of arithmetic and say, e.g., that a $v_{\rm abs}$ measurement *increases* from −25,000 to −15,000 km s^{-1}, while the simplistic interpretation of such a variation suggests that the corresponding location of maximum absorption *decreases* from outflow *kinematic* velocities of 25,000 down to 15,000 km s^{-1} (see § 3.1.2).

3.1.1. *Presentation of $v_{\rm abs}$ Measurements*

In Figure 4 (*top*) we show $v_{\rm abs}$ measurements for the local SN Ia sample for the Ca II λ3945 feature as a function of phase and ordered according to their decline rate: $\Delta m_{15}(B) < 1.0$ ("slow decliners"; *downward-pointing triangles*), $1.0 \leq \Delta m_{15}(B) \leq 1.7$ (*circles*), and $\Delta m_{15}(B) > 1.7$ ("fast decliners"; *upward-pointing triangles*). For the few objects showing a double-absorption Ca II feature (tagged "blue" and "red" according to wavelength; see § 3.3 and Table 5), we plot only the redder component. We invert the ordinate ($v_{\rm abs}$) axis for consistency with previously published measurements, which usually associate the absorption blueshifts with positive velocities.

The absorption velocities for Ca II λ3945 reveal two $v_{\rm abs}$ sequences at premaximum phases: one sequence shows a steady increase in $v_{\rm abs}$ from a minimum of $\gtrsim$−25,000 km s^{-1} at the earliest observed phases ($\lesssim$−10 days) to approximately −15,000 km s^{-1} at B-band maximum, after which the evolution is more gradual or even constant. A second sequence is located at less negative $v_{\rm abs}$ ($v_{\rm abs} \gtrsim$ −15,000 km s^{-1}) and remains almost constant around −12,000 km s^{-1}. This sequence corresponds to red Ca II absorption components that have a blue counterpart, and the resulting

TABLE 5
ABSORPTION VELOCITIES IN LOCAL SNE IA (10^3 km s^{-1})

	Ca II λ3945[b]				
Phase[a]	Blue Absorption	Red/Single Absorption	S II λ5454	S II λ5640	Si II λ6355
		1994D[c]			
−4	-22.0 ± 0.3	-13.3 ± 0.3	-9.7 ± 0.2	-11.5 ± 0.2	-11.7 ± 0.2
−3	-20.0 ± 0.3	$-11.9^{+1.1}_{-1.0}$	-9.4 ± 0.2	-11.3 ± 0.2	-11.5 ± 0.2
−2	-19.7 ± 0.3	$-11.6^{+1.1}_{-1.0}$	-9.4 ± 0.2	-11.2 ± 0.2	-11.4 ± 0.2
+2	...	...	-8.6 ± 0.2	-10.2 ± 0.2	-11.1 ± 0.2
+3	-17.2 ± 0.3	-11.3 ± 0.3	-8.2 ± 0.2	-9.6 ± 0.2	-10.9 ± 0.2
+10	...[d]	...[d]	...	-8.3 ± 0.2	-10.4 ± 0.2

NOTE.—Table 5 is published in its entirety in the electronic edition of the *Astronomical Journal*. A portion is shown here for guidance regarding its form and content.
[a] Rest-frame days from B-band maximum, rounded to closest whole day.
[b] The $v_{\rm abs}$ measurements for Ca II λ3945 are separated into blue and red components (when a double absorption is present). Both red and single-absorption velocities are reported in the same column.
[c] For SN 1994D there is evidence for several blue Ca II components (see Fig. 3 of Hatano et al. 1999). In the blue column we report the absorption velocity corresponding to the bluest component.
[d] Insufficient wavelength coverage.

TABLE 6
ABSORPTION VELOCITIES IN ESSENCE HIGH-z SNe Ia (10^3 km s^{-1})

IAU NAME	PHASE[a]	Ca II λ3945[b]		S II λ5454	S II λ5640	Si II λ6355
		Blue Absorption	Red/Single Absorption			
2003jt[c]	+3	-23.7 ± 3.1	-17.7 ± 3.1	...	...	...
2003ju	−8	...[c]	...[c]	...	-10.8 ± 3.0	-16.7 ± 3.0
2003ju	+18	...	...	...	...	-8.8 ± 3.1
2003jv	−2	...	...	-9.6 ± 0.5	-12.1 ± 0.5	-11.6 ± 0.5
2003jw[d]	−6	...	-18.9 ± 0.7	...	-11.2 ± 0.8	-11.5 ± 1.4
2003jy[d]	−10	...	-22.2 ± 0.7	-11.7 ± 0.8	-13.0 ± 0.8	-11.4 ± 0.9

NOTE.—Table 6 is published in its entirety in the electronic edition of the *Astronomical Journal*. A portion is shown here for guidance regarding its form and content.

[a] Rest-frame days from B-band maximum, rounded to closest whole day.

[b] The v_{abs} measurements for Ca II λ3945 are separated into blue and red components (when a double absorption is present). Both red and single-absorption velocities are reported in the same column.

[c] Insufficient wavelength coverage.

[d] VLT spectra reduced with the two-dimensional restoration method of Blondin et al. (2005).

contamination biases the measurements to higher v_{abs} (see § 3.3). The scatter in v_{abs} decreases with SN phase, regardless of decline rate, from approximately $\pm$7000 km s^{-1} at -10 days to $\lesssim\pm$3000 km s^{-1} at +20–30 days. The fast decliners overlap significantly with the other SNe Ia and thus cannot be used to discriminate between subluminous and overluminous objects, contrary to claims made by Lidman (2004). Within the $\Delta m_{15}(B) < 1.0$ sample, two objects (SN 1990O and 1999ee) form a v_{abs} sequence at more negative velocities, suggesting higher explosion kinetic energies. The other eight slow-declining SNe Ia cannot be distinguished from those with $\Delta m_{15}(B) \geq 1.0$ at all phases.

In Figure 4 (*bottom*) we overplot the v_{abs} measurements for our sample of high-z ($0.16 \leq z \leq 0.64$) SNe Ia, again ordered according to their decline rate: $\Delta m_{15}(B) < 1.0$ (*stars*) and $1.0 < \Delta m_{15}(B) < 1.7$ (*squares*). The time evolution of v_{abs} for Ca II λ3945 in our high-z sample is similar to that for the local SNe Ia: a steady increase from $\gtrsim -25{,}000$ km s^{-1} at very early phases ($\lesssim -10$ days) to approximately $-15{,}000$ km s^{-1} at maximum and a more gradual postmaximum increase. Again, the slow-declining high-z SNe Ia cannot be distinguished.

Because this Ca II feature is a few hundred angstroms wide, it likely overlaps with other lines. To illustrate and assess the magnitude of such a line overlap, we show in Figure 5 (*top*) synthetic SYNOW (Fisher et al. 1999) spectra for SN 1994D at -10, -1, and +10 days from B-band maximum (Branch et al. 2005; *solid line*), as well as the relative contribution from Ca II (*dotted line*), S II (*short-dashed line*), and Si II (*long-dashed line*). (All spectra are normalized to the adopted blackbody continuum energy distribution.) We see that the strong Ca II λ3945 absorption feature (including the blue absorption; see § 3.3) is contaminated at all phases, predominantly by Si II λ3858 (gf-weighted mean rest-frame wavelength). However, it is only around and past maximum that the v_{abs} measurement is affected by the Si II λ3858 absorption: at maximum (+10 days), v_{abs} is biased to less (more) negative values. Despite this corrupting effect, the Ca II λ3945 line is the major contributor to the wide absorption trough seen at $\sim$3750 Å for all phases $\lesssim$2 weeks from B-band maximum.

In Figure 6 (*top*) we reproduce Figure 4 for Si II λ6355, showing the v_{abs} measurements for the local SN Ia sample. The v_{abs} evolution for this feature is comparable to that for Ca II λ3945, although values are less negative at all phases by $\sim$5000 km s^{-1} (see also Fig. 5 and § 3.1.2). The fast-declining SNe Ia form, on average, a sequence of less negative v_{abs} at postmaximum phases, but this sequence separates only at $t \gtrsim +20$ days from the $1.0 \leq \Delta m_{15}(B) \leq 1.7$ objects. The higher scatter in the slow-declining SNe Ia causes an overlap with the fast-declining ones at all phases. We are lacking data at $t \gtrsim +20$ days to make a clear distinction between the slowest and fastest decliners of our sample. At these late phases, however, the optical spectra of SNe Ia are dominated by lines of iron-group elements (mainly Co II and Fe II), and the Si II λ6355 feature suffers from increasing line blending. Note that the Si II λ6355 absorption profile is

TABLE 7
EMISSION-PEAK VELOCITIES IN LOCAL SNe Ia (10^3 km s^{-1})

Phase[a]	Ca II λ3945	S II λ5454	S II λ5640	Si II λ6355
		1994D		
−4	-1.4 ± 0.3	-6.0 ± 0.2	...	-0.5 ± 0.2
−3	-1.3 ± 0.3	-5.4 ± 0.2	...	-0.9 ± 0.2
−2	-1.2 ± 0.3	-5.3 ± 0.2	...	-1.1 ± 0.2
+2	-1.4 ± 0.3	-4.6 ± 0.2	-2.4 ± 0.2	-1.4 ± 0.2
+3	...	-4.1 ± 0.2	-2.2 ± 0.2	-0.8 ± 0.2
+10	...[b]	...	-5.7 ± 0.2	...

NOTE.—Table 7 is published in its entirety in the electronic edition of the *Astronomical Journal*. A portion is shown here for guidance regarding its form and content.

[a] Rest-frame days from B-band maximum, rounded to closest whole day.

[b] Insufficient wavelength coverage.

TABLE 8
EMISSION-PEAK VELOCITIES IN ESSENCE HIGH-z SNe Ia (10^3 km s^{-1})

IAU Name	Phase[a]	Ca II λ3945	S II λ5454	S II λ5640	Si II λ6355
2003jt[c]	+3	-5.5 ± 3.1	...	...	...
2003ju	−8	...[b]	-4.2 ± 3.0	-4.2 ± 3.0	-3.4 ± 3.0
2003ju	+18	-3.4 ± 3.8	...	...	...
2003jv	−2	-2.8 ± 0.3	-6.3 ± 0.5	-3.3 ± 0.5	-3.0 ± 0.5
2003jw[c]	−6	-1.5 ± 0.7	...	-1.8 ± 0.8	-4.1 ± 1.4
2003jy[c]	−10	-1.4 ± 0.7	...	-7.8 ± 0.8	-4.5 ± 0.9

NOTE.—Table 8 is published in its entirety in the electronic edition of the *Astronomical Journal*. A portion is shown here for guidance regarding its form and content.

[a] Rest-frame days from B-band maximum, rounded to closest whole day.

[b] Insufficient wavelength coverage.

[c] VLT spectra reduced with the two-dimensional restoration method of Blondin et al. (2005).

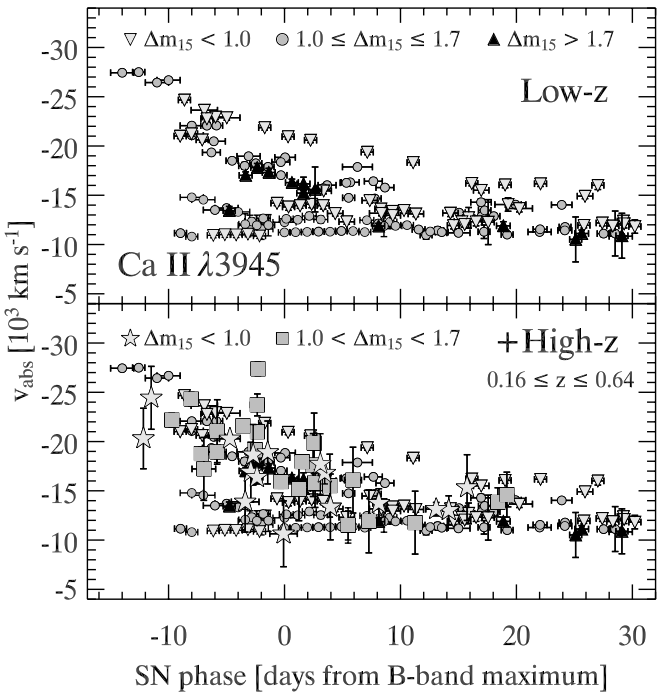

FIG. 4.—*Top*: Absorption velocities for Ca II λ3945 in local SNe Ia for three different $\Delta m_{15}(B)$ ranges. If a double absorption is present, only the redder component is plotted. *Bottom*: High-z data overplotted. [*See the electronic edition of the Journal for a color version of this figure.*]

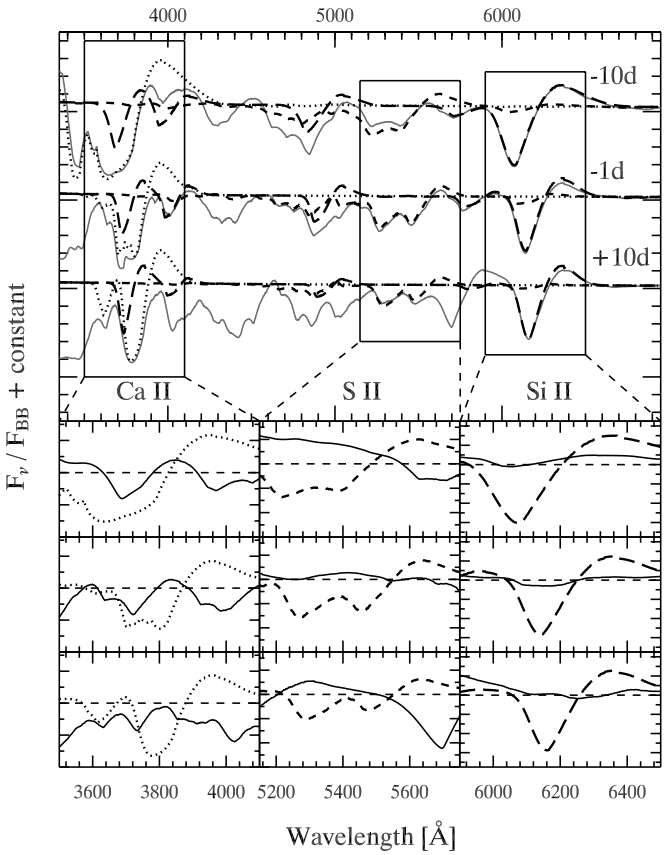

FIG. 5.—*Top*: SYNOW models of SN 1994D at −10, −1, and +10 days (*solid lines*), along with the contributions from Ca II (*dotted lines*), S II (*short-dashed lines*), and Si II (*long-dashed lines*). The fluxes (per unit frequency, F_ν) are normalized to the underlying blackbody continuum (F_{BB}). Unlike Branch et al. (2005), we have not included (weak) contributions from C II in the −10 days spectrum. *Bottom*: Close-up of the Ca II λ3945 (*left*), S II $\lambda\lambda$5454, 5640 (*middle*), and Si II λ6355 (*right*) features. The lines are the same as for the top panel, except that now the solid lines correspond to the contribution from all *other* ions. The fluxes are again in F_ν and normalized to F_{BB} (*dashed line*). [*See the electronic edition of the Journal for a color version of this figure.*]

sometimes unusually flat and extended (see, e.g., SN 1990N at −14 and −13 days with $v_{abs} \sim -20{,}000$ km s^{-1}; see also SN 2001el in Mattila et al. 2005), perhaps due to contamination from C II λ6580 forming in a high-velocity shell (Fisher et al. 1997; see also Mazzali 2001). The high-z sample (Fig. 6, *bottom*) reveals similar properties. Note that Si II λ6355 falls outside the optical spectral range for $z \gtrsim 0.4$; the highest redshift at which we were able to measure v_{abs} for this feature was $z = 0.428$.

We now turn to the weakest lines in our study, the S II $\lambda\lambda$5454, 5640 features, for which we show the time evolution of v_{abs} in Figure 7. Compared to Ca II λ3945 and Si II λ6355, v_{abs} values for the S II lines are less negative at all phases (always greater than −13,000 km s^{-1} for 5454 Å and −15,000 km s^{-1} for 5640 Å), with a nearly constant and smaller increase with phase. These optically thinner lines are increasingly contaminated by those of iron-group elements at $t \gtrsim 2$ weeks, becoming unnoticeable at later phases; this explains the lack of data at late phases in Figure 7. Three of the $1.0 \leq \Delta m_{15}(B) \leq 1.7$ points for S II λ5640 at $t \sim -10$ days, associated with SN 2002bo (Benetti et al. 2004), lie at more negative velocities ($<-13{,}000$ km s^{-1}) than the bulk of our sample. Several points at phases between maximum and +10 days, associated with SN 1994M (Gómez et al. 1996), also have more negative velocities than the rest of our sample data. This may result from line blending, although our SYNOW investigation (see Fig. 5, *bottom middle panels*) suggests this overlap to be weak or absent.

Alternatively, the S II v_{abs} measurements might be influenced by the overlap between the 13 individual S II features in the range 5300–5700 Å (Kurucz & Bell 1995). For example, distinct intrinsic excitation temperatures and formation mechanisms for one transition could cause its optical depth to vary differently from that of others and thus modulate, at selected phases, the observed location of maximum absorption in the total profile. Note that the Ca II λ3945 and Si II λ6355 features are the result of transitions corresponding to a single multiplet and will not be affected by this issue.

Interestingly, fast decliners at positive phase show the least negative S II $\lambda\lambda$5454, 5640 v_{abs} values with a lower limit of approximately −8000 km s^{-1}, combined with the most pronounced v_{abs} gradient with phase among the different $\Delta m_{15}(B)$ subgroups. Provided the phase is known accurately, these two S II features can be used to discriminate between fast and slow decliners at post-maximum phases.

3.1.2. *Interpretation of v_{abs} Measurements*

We now investigate the causes of the variations in line profile shapes and v_{abs} values for our optical diagnostics. We base our discussion on synthetic line profiles computed with CMFGEN (Hillier & Miller 1998), a steady state, one-dimensional, non–local thermodynamic equilibrium (non-LTE) model atmosphere code that solves the radiative transfer equation in the comoving frame, subject to the constraints of radiative and statistical equilibria. Because CMFGEN is at present not strictly adequate for SN Ia conditions (no chemical stratification, no γ-ray energy deposition, and neglect of relativistic effects apart from first-order Doppler corrections; see Dessart & Hillier [2005a] for details), these results are merely illustrative; nonetheless, they provide a new insight into the sites of optical line and continuum formation, corresponding in this example to a low-luminosity SN Ia ("SN 1991bg–like") near maximum light.

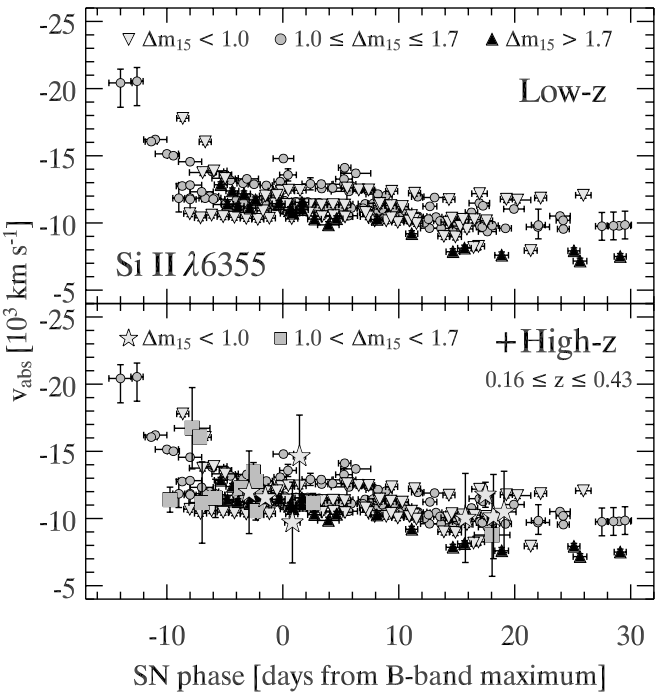

FIG. 6.—*Top*: Absorption velocities for Si II λ6355 in local SNe Ia for three different $\Delta m_{15}(B)$ ranges. *Bottom*: High-*z* data overplotted. [*See the electronic edition of the Journal for a color version of this figure.*]

TABLE 9
CMFGEN MODEL PARAMETERS

Model Parameter	Parameter Value
Radius, R_0 (cm)	4×10^{14} ($\sim$5750 $R_\odot$)
Velocity at R_0, v_0 (km s^{-1})	5000
Luminosity, L_0 ($L_\odot$)	8×10^8
Density, ρ_0 (g cm^{-3})	2×10^{-11}
Density gradient, n [in $\rho(r) = \rho_0(R_0/r)^n$]	7
Turbulent velocity, $v_{\rm turb}$ (km s^{-1})	90
Mass Fraction	
C	0.12
O	0.63
Mg	0.1
Si	0.1
S	0.05
Ca	0.0001
Fe	0.0014
Ni	0.001

The SN Ia conditions are epitomized here by the absence of hydrogen and helium in the outflow and thus the dominance of metal species. Their mass fractions, alongside basic model parameters, are listed in Table 9. Note that the continuum optical depth at the base radius R_0 is $\sim$50.

We show in Figure 8 the synthetic line profiles for Ca II λ3934 (*left*), Si II λ6347 (*middle*), and S II λ5432 (*right*) computed under such model assumptions. At the bottom of each panel, and following Dessart & Hillier (2005a, 2005b), we show gray-scale

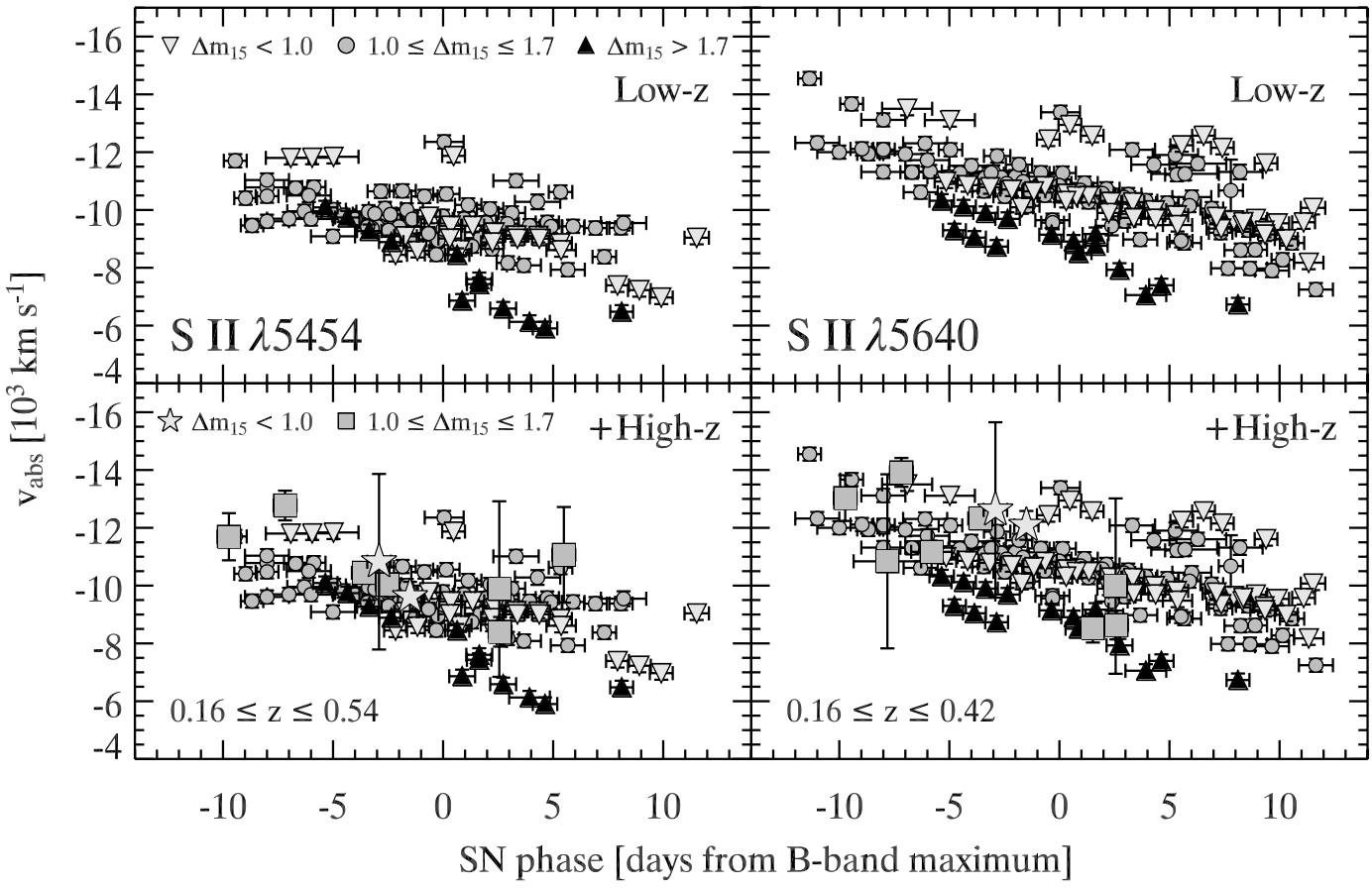

FIG. 7.—*Top*: Absorption velocities for S II λ5454 (*left*) and S II λ5640 (*right*) in local SNe Ia for three different $\Delta m_{15}(B)$ ranges. *Bottom*: High-*z* data overplotted. [*See the electronic edition of the Journal for a color version of this figure.*]

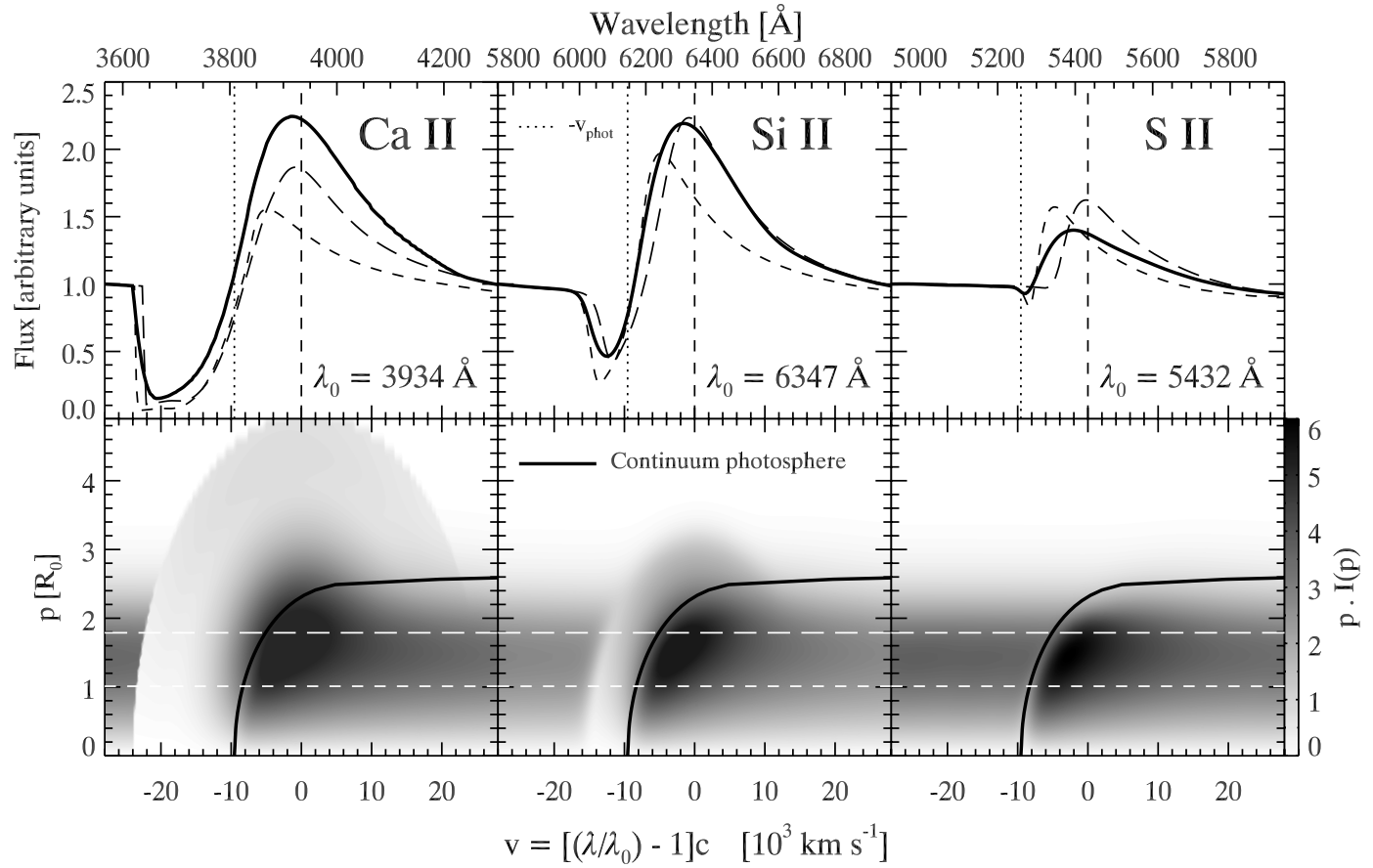

FIG. 8.—P Cygni profiles of Ca II λ3934, S II λ5432, and Si II λ6347 in a CMFGEN model of a low-luminosity SN Ia near maximum brightness, with density exponent $n = 7$, revealing the sites at the origin of synthetic line profile flux, and the resulting blueshift of the P Cygni profile emission peak. *Bottom*: Gray-scale image of the quantity $pI(p)$ as a function of p and classical Doppler velocity $v = [(\lambda/\lambda_0) - 1]c$, where p is the impact parameter and $I(p)$ is the emergent specific intensity along p (at v). Here R_0 is the base radius of the CMFGEN radial grid where the continuum optical depth $\tau_{\rm cont} \approx 50$; a photosphere thus exists in this model configuration, corresponding to a velocity of 9550 km s^{-1}. Here λ_0 is the rest wavelength of the transition and c is the speed of light in a vacuum. The overplotted solid curve gives the line-of-sight velocity location where the integrated continuum optical depth at 5500 Å, along z and at a given p, equals 2/3. (Note that the photospheric velocity quoted above, not projected, is found at the point on this curve with $p = 0$, which also corresponds to a depth $z = 1.91R_0 = v_{\rm phot}/v_0$; see Table 9.) In the (p, z) plane, this curve has a similar shape but is more circular for negative z, as shown for a synthetic Hα profile for a SN II in Fig. 10 of Dessart & Hillier (2005b). The dashed lines are for $p = (1,\ 1.8)$. *Top*: Solid curves indicate the line profile flux obtained by summing $pI(p)$ over the range of p; dashed curves indicate the velocity profile of $pI(p)$ for two p-rays, at $p = (1,\ 1.8)$. The vertical dotted lines correspond to the (continuum) photospheric velocity. The profiles have been normalized to unity at the inferior boundary of the plotted velocity range, where the line optical depth is zero. See Dessart & Hillier (2005a, 2005b) for a detailed and pedagogical explanation of these plots in the context of SNe II.

images in the (v, p) plane of the fluxlike quantity $pI(p)$, where $v = [(\lambda/\lambda_0) - 1]c$ is the classical Doppler velocity, p is the impact parameter in units of R_0, and $I(p)$ is the specific intensity at p. The photosphere, corresponding to $\tau_{\rm cont} = 2/3$ at 5500 Å, is shown as a solid line in the bottom panels. The dominance of the (gray) electron-scattering opacity makes the corresponding radius essentially wavelength-independent over the range considered here; see, e.g., § 4.2 and Figures 7–9 of Dessart & Hillier (2005b). The sum over p of the quantity $pI(p)$ at v corresponds to the total line flux at v, shown at the top of each panel (*solid line*). Note that for each line, we select a single transition to avoid the corrupting effect of line overlap stemming from other transitions of the same or different species.

Let us first focus on the absorption trough, controlling the resulting $v_{\rm abs}$, of such synthetic line profiles. For Ca II λ3934 we see that the trough is nearly saturated with essentially no residual flux down to approximately $-22{,}000$ km s^{-1}, while Si II λ6347 shows a maximum absorption at a less negative velocity of $-12{,}000$ km s^{-1}; S II λ5432 is the weakest line of the three, with a very modest absorption and extent, located at approximately -9500 km s^{-1}.

We thus reproduce here the general trend shown in Figures 4–7 and presented in § 3.1.1: absorption velocities for Ca II λ3945 are more negative by several 1000 km s^{-1} at any given phase than those for S II $\lambda\lambda$5454, 5640 and Si II λ6355, because it remains optically thick out to larger radii (i.e., lower densities and higher expansion velocities). Indeed, this feature is the result of a blend of Ca II K (3933.66 Å) and H (3968.47 Å) transitions, both corresponding to the same $4s\ ^2S$–$4p\ ^2P^0$ multiplet, linking the ground state and low-lying upper levels (just 3 eV above the ground state). Despite the low $\log(gf)$ value of the transition and the considerably lower calcium abundance compared to silicon and sulfur in our model (by factors of 1000 and 500, respectively), the high Ca II ground-state population in this parameter space translates into a very large line optical depth ($\tau_{\rm line} \propto \kappa_{\rm line}\rho_{\rm ion}$). The sample Si II and S II lines result, however, from higher level transitions, less populated, which translate into systematically lower optical depths and less negative $v_{\rm abs}$ values, the more so for the S II lines. Also, at a given phase, the maximum absorption is further to the blue in S II λ5640 than in S II λ5454, which likely results from differences in the atomic properties of each transition.

Despite the assumed homogeneity and smooth density distribution of the CMFGEN model, a scatter in v_{abs} between line diagnostics is not only present but also large and comparable to the observed scatter; inferring the presence, at a given phase, of chemical stratification in the SN outflow thus requires careful analysis, with a detailed and accurate account of all line optical depth effects (Stehle et al. 2005). This argues for caution in the interpretation of v_{abs} measurements, since one sees the numerous competing effects arising from differences in the atomic-transition properties, chemical abundances, density, and velocity distribution; additional corrupting effects such as line overlap are discussed later in this paper.

In Figure 8 we also see that $|v_{abs}|$ underestimates the velocity of the photosphere for the weak, optically thinner S II λ5432 line. The physical origin of this effect is given in Dessart & Hillier (2005b) and stems from the steep density gradient in SN atmospheres [$\rho(r) \propto r^{-n}$]: isovelocity curves are at constant v [depth z in the (p, z) plane], but the density varies as $1/r^n$. Thus, at fixed z, the density drops fast for increasing p, at the same time reducing the probability of line scattering and/or absorption. In practice, the location of maximum absorption along a p-ray shifts to larger depths (z closer to zero) for increasing p, showing overall the same curvature as seen for the photosphere (see overplotted curve). Along a given p-ray, the location of maximum absorption is always exterior to the photosphere along that ray (the line opacity comes on top of the default continuum opacity) but shifts toward line center for increasing p. As a consequence, the total line profile, which results from the contribution at all impact parameters, shows a maximum absorption at a velocity v_{abs}, the magnitude of which can be higher *or* lower than the photospheric value v_{phot}. This offset between $|v_{abs}|$ and v_{phot} is determined primarily by the magnitude of the line optical depth. As we move from Ca II λ3934 to Si II λ6347 and S II λ5432, the line optical depth decreases, and the corresponding absorption velocity is closer to zero.

Note that the comparison with the photospheric velocity of the SN Ia outflow is not necessarily meaningful. First, electron scattering, which provides the dominant source of continuum opacity in ionized hydrogen-free and helium-free outflows, corresponds to a small mass absorption coefficient due to the high mean molecular weight of the gas ($\kappa_e \lesssim 0.05$ cm^2 g^{-1}, a factor at least 10 times smaller than in hot star outflows). Second, the outflow density decreases with the cube of the time, following the homologous expansion of the SN Ia, so that the outflow becomes optically thin in the continuum after about 10 days past explosion; the concept of a photosphere then becomes meaningless. The alternative definition (not adopted here) of the photosphere as the location where the total (line and continuum) inward integrated optical depth is 2/3 changes this conception somewhat: the ubiquitous presence of lines makes the photospheric radius (and velocity) highly dependent on wavelength and thus nonunique and ambiguous (see Höflich et al. 1993; Spyromilio et al. 1994; Höflich 1995; Pinto & Eastman 2000).

3.2. *Emission-Peak Velocities*

Large negative v_{peak} values are common in optical line profiles of SN II spectra, explained for the first time by Dessart & Hillier (2005a); the root cause is the strong SN outflow density gradient. Because such a property is common to both SNe Ia and SNe II, such peak-emission blueshifts are also expected in SN Ia line profiles. Using the same approach as before for v_{abs}, we present in § 3.2.1, for the first time, a census of v_{peak} measurements, using our large sample of local and high-z SN Ia spectra. We then comment on these results in § 3.2.2, using the CMFGEN model presented in § 3.1.2.

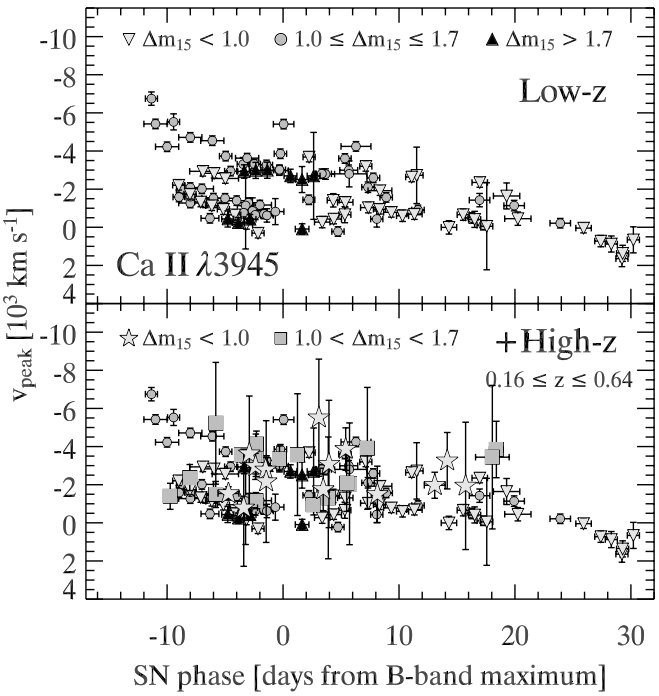

FIG. 9.—*Top*: Emission-peak velocities for Ca II λ3945 in local SNe Ia for three different $\Delta m_{15}(B)$ ranges. *Bottom*: High-z data overplotted. [*See the electronic edition of the Journal for a color version of this figure.*]

3.2.1. *Presentation of v_{peak} Measurements*

Keeping the same structure as for previous figures displaying v_{abs} measurements, we show in Figure 9 the phase-dependent v_{peak} measurements for the Ca II λ3945 feature in local SNe Ia (*top*) and all sampled SNe Ia (*bottom*), separating objects according to their decline-rate parameter, $\Delta m_{15}(B)$. As for SNe II, all v_{peak} measurements for Ca II λ3945 at $\lesssim$+20 days are negative; that is, the peak emission is blueshifted with respect to the rest wavelength of the line, increasing with phase from approximately -6000 km s^{-1} (at -10 days) up to -1000 km s^{-1} (+20 days). The scatter is, however, significant. Moreover, at any phase, near-zero values are found. As previously for v_{abs} measurements, Si II λ3858 modifies the Ca II intrinsic line profile shape but now introduces, at all phases, a blueshift of the emission peak of the 3945 Å feature (Fig. 5, *left*), likely influencing the scatter and the magnitude of v_{peak} values (see § 3.2.2). A few points at $\gtrsim$+25 days (corresponding to the spectroscopically peculiar SN 1999aa; Li et al. 2001a) show a counterexample to the above trend, with $v_{peak} > 0$. At these phases, however, Ca II λ3945 is increasingly contaminated from lines of iron-group elements, and the measurements of v_{peak} at these phases are highly uncertain. Note that v_{peak} measurements for the high-z sample are consistent with the trend in the local sample, both qualitatively and quantitatively (Fig. 9, *bottom*).

A similar pattern is also found for Si II λ6355, for both local and high-z SNe Ia (Fig. 10), although the measurement errors for the latter are $\sim$1000 km s^{-1}. Unlike for the Ca II feature, these measurements are free of sizable line overlap (see § 3.1.1) and therefore represent a genuine intrinsic blueshift of peak emission of Si II λ6355. Note that v_{peak} for the slow-declining (overluminous) SNe Ia is slightly more negative (by $\sim$1000 km s^{-1}), on average, than for the fast-declining (underluminous) objects. Since the magnitude of the emission-peak blueshift scales with the expansion velocity of the ejecta (see the end of this section), this dependence supports the idea that slow-declining SNe Ia correspond to higher kinetic energy explosions (Mazzali et al. 1998;

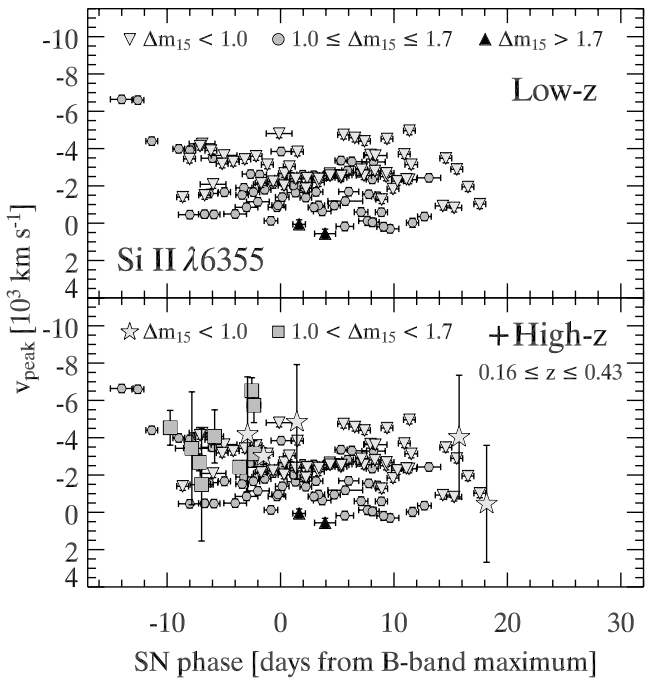

FIG. 10.—Same as Fig. 9, but for Si II λ6355. [*See the electronic edition of the Journal for a color version of this figure*.]

Leibundgut 2000). The two points with $v_{peak} < -6000$ km s^{-1} at $t < -10$ days correspond to SN 1990N, for which the v_{abs} measurements at these phases are also more negative (Fig. 6).

We finally turn in Figure 11 to the v_{peak} measurements for the S II λ5454, 5640 features. We start with the panels on the right, which show that the S II λ5640 data points, for both the local and high-z samples, follow a similar pattern of increasing values with phase as for the Ca II and Si II features, with velocity shifts always negative but now reaching down to −8500 km s^{-1} at approximately −10 days. We associate the large scatter of data points with contamination by Si II λ5972 at premaximum phases and Na I D λ5892 at postmaximum phases. Note that for the high-z sample, an uncertainty of about 3000 km s^{-1} is introduced when the SN redshift is determined via cross-correlation with local SN Ia spectral templates (see Table 1). For S II λ5454 (*left*) we find, on average, a steady increase of v_{peak} with phase, from −8500 km s^{-1} at −10 days to −4000 km s^{-1} at +10 days, but with a clear dichotomy according to the $\Delta m_{15}(B)$ parameter: fast decliners show systematically faster increasing and less negative values, related to the modest expansion velocity of their outflows and the larger (comoving) recession velocity of the photoemitting layers in the SN ejecta. The low scatter of data points, due to the absence of sizable line overlap, makes this distinction clear and suggests that, as before from v_{abs} measurements, the blueshift of peak emission at postmaximum phases can now also be used to isolate fast-declining SNe Ia, provided the SN phase is accurately known.

To conclude this section on the v_{peak} measurements, we show in Figure 12 the values for S II λ5454, but this time normalized to

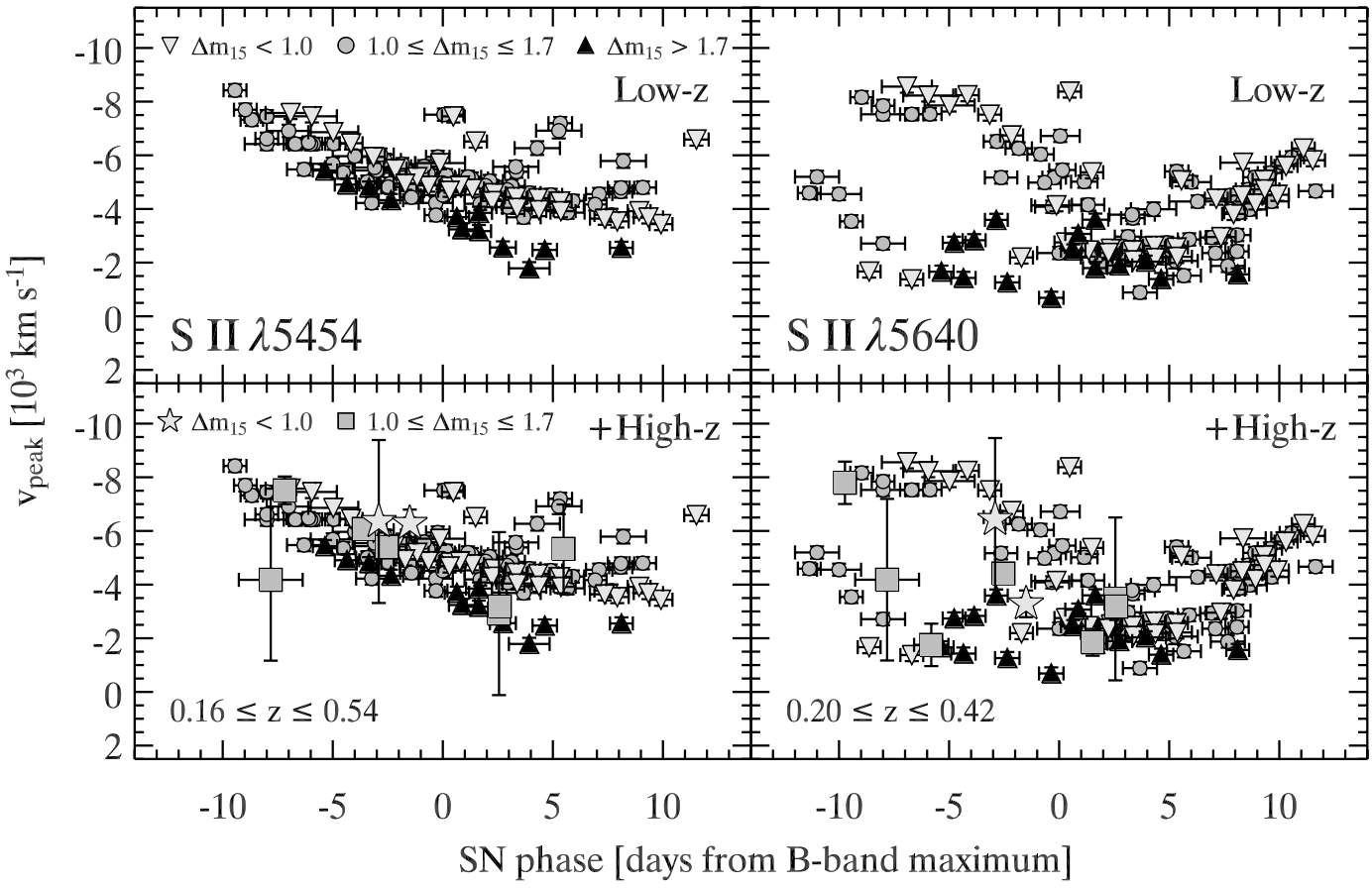

FIG. 11.—*Top*: Emission-peak velocities for S II λ5454 (*left*) and S II λ5640 (*right*) in local SNe Ia for three different $\Delta m_{15}(B)$ ranges. *Bottom*: High-z data overplotted. [*See the electronic edition of the Journal for a color version of this figure*.]

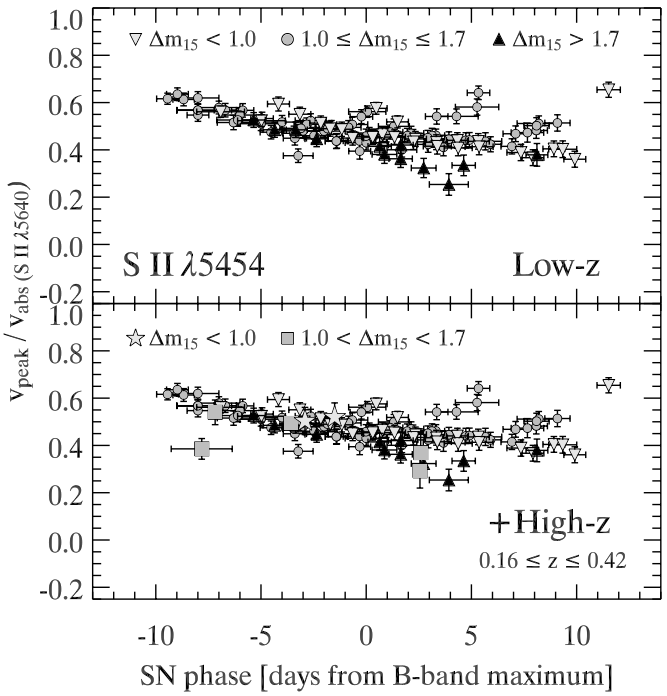

FIG. 12.—*Top*: Emission-peak velocities for S II λ5454 normalized to the S II λ5640 absorption velocities. *Bottom*: High-*z* data overplotted. [*See the electronic edition of the Journal for a color version of this figure*.]

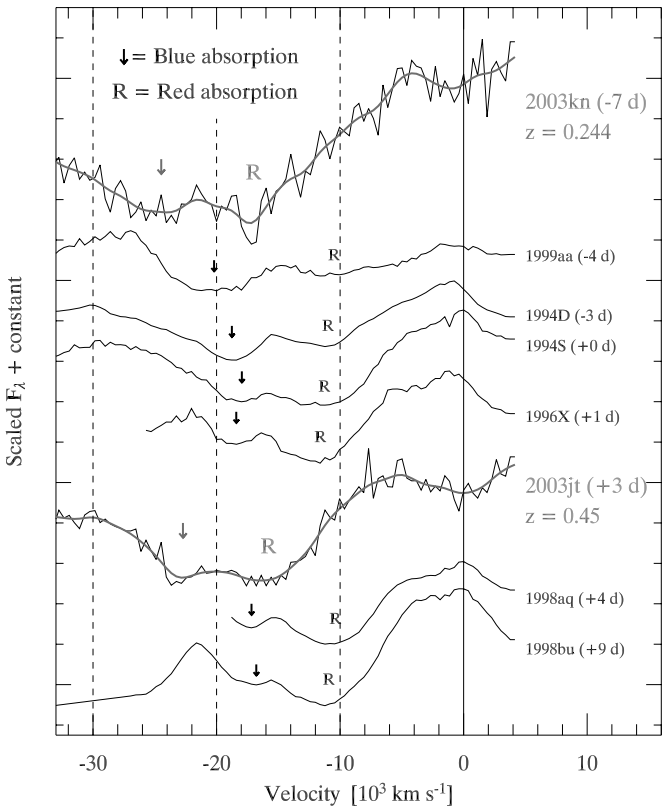

FIG. 13.—Double-absorption features in Ca II λ3945. Two of our high-*z* SNe Ia also show a double-absorption feature. The thick line overplotted on these spectra corresponds to their smoothed version (see § 2.1). Note the apparent approximately −5000 km s^{-1} offset of the SN 2003jt spectrum with respect to local SNe Ia at similar phases, probably due to an error in the SN redshift (determined via cross-correlations with local SN Ia spectra; Matheson et al. 2005). The solid vertical line corresponds to 3945 Å, while the dashed vertical lines correspond to blueshifts of 10,000, 20,000, and 30,000 km s^{-1}. [*See the electronic edition of the Journal for a color version of this figure*.]

$v_{abs,5640}$ at the same phase, a quantity that closely matches, at early times, the photospheric velocity of the flow (Fig. 8). For both local and high-*z* SNe Ia, this ratio covers the 0.2–0.7 range and thus represents a significant shift of a line profile, comparable to the shift identified in the measurement of the absorption velocity. The time evolution of v_{peak}/v_{abs} has a flatter slope than the corresponding v_{peak} sequence of Figure 11 (*left*), suggesting that the magnitude of emission blueshift is a good tracer of the expansion velocity.

3.2.2. *Physical Origin of the Emission-Peak Blueshift*

To investigate the origin of the observed blueshift of peak emission, let us go back to the left panels of Figure 8 and study the sites of emission in the Ca II λ3934 line. As in the standard cartoon of P Cygni profile formation, one can view a significant amount of flux arising from the sidelobes, corresponding to regions with $p > p_{lim} \approx 3R_0$; this defines the spatial extent of the (continuum) photodisk. Despite the weaker emission at such distances from the photosphere, the total contribution is much bigger, because it involves a larger and optically thinner emitting volume. Contrary to such a heuristic P Cygni profile formation, a significant amount of emission also arises from the region with $p < p_{lim}$; this more restricted volume is, however, affected by continuum optical depth effects, since it resides partly within the photosphere (*solid line*). Although this latter emission source appears in the blue side of the profile, the larger contribution from the lobes leads to a relatively symmetric emission peak.

Moving to the optically thinner Si II λ6355 line (cf. Fig. 8, *middle panels*), we now see that the relative (symmetric) emission contribution from the lobe is lower compared to that arising from within the limbs of the photodisk, leading to a more pronounced blueshift of peak emission. This situation becomes even more extreme in the case of S II λ5432 (Fig. 8, *right panels*), wherein no sidelobe emission is present; the resulting P Cygni profile shows a strongly blueshifted centroid, corresponding to a sizable fraction of the velocity at maximum absorption. For this very optically thin line, continuum optical depth effects are severe.

These synthetic line profiles are computed by accounting solely for the opacity of the chosen line (plus all sources of continuum opacity); thus, they lift any ambiguity brought on by line overlap. In view of these results, the large and scattered observed (negative) v_{peak} measurements for Ca II λ3945 are likely caused by line overlap, the most likely candidate being Si II λ3858. However, the measured and sizable blueshifts for the Si II and S II lines are indeed expected theoretically; CMFGEN computations also predict the larger blueshift velocity (more negative v_{peak}) for the optically thinner S II lines, compared to either Si II or Ca II diagnostics.

Interestingly, Kasen et al. (2002) argued that such blueshifted emission must stem from peculiar effects (for example, of a non-LTE nature), rather than from modulations of the line source function or optical depth. It now seems that their combined assumptions of a sharp photosphere, the neglect of continuum opacity, and a pure scattering source function enforce the symmetry of P Cygni profile emission; here CMFGEN demonstrates that such assumptions may be invalid for a number of lines, particularly at epochs in which the ejecta are optically thick in the continuum.

3.3. *Double-Absorption Features in* Ca II λ3945

Double-absorption features in Ca II are frequently observed in local SNe Ia, usually in the near-infrared lines at 8498, 8542, and

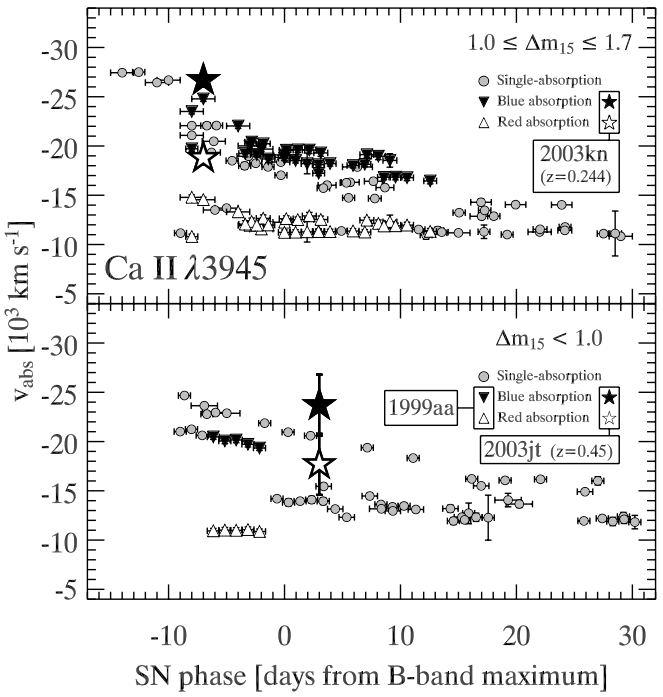

FIG. 14.—Absorption velocities for Ca II λ3945 in single- and double-absorption features (blue and red components) for objects with $1.0 \leq \Delta m_{15}(B) \leq 1.7$ (*top*) and $\Delta m_{15}(B) < 1.0$ (*bottom*). Also shown are $v_{\rm blue}$ and $v_{\rm red}$ absorption velocities for SN 2003kn ($z = 0.244$) and SN 2003jt ($z = 0.45$).

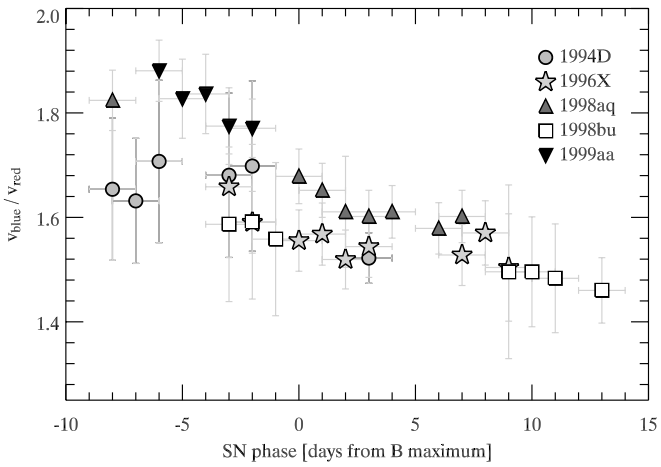

FIG. 15.—Time evolution of the ratio of $v_{\rm abs}$ for the blue and red components of the Ca II λ3945 absorption feature in five local SNe Ia. [*See the electronic edition of the Journal for a color version of this figure.*]

8662 Å (see, e.g., Gerardy et al. 2004; Mazzali et al. 2005; Mattila et al. 2005). Gerardy et al. (2004) suggest the interaction of a circumstellar shell within the progenitor system, but Kasen et al. (2003) propose a departure from sphericity in the explosion, inferred from polarization measurements of SN 2001el (Wang et al. 2003). Gerardy et al. (2004) also discuss the possibility of detecting such double-absorption Ca II absorption features in the λ3945 doublet; alternatively, such identification could be influenced by the overlap of the bluer component with Si II λ3858 (see Fig. 5), predicted to dominate past ∼1 week before maximum (Höflich 1995; Höflich et al. 1998; Lentz et al. 2000). The association of the blue component in Ca II λ3945 with high-velocity Ca II absorption is uncertain, and we therefore prefer referring to the *observed* blue/red, rather than the *interpreted* high-velocity/low-velocity components as commonly used in the literature.

Here line-profile measurements of Ca II λ3945 reveal possible double-absorption features for 6 (out of 22) local SNe Ia and, for the first time, for 2 (out of 34) high-z SNe Ia (Table 3), SN 2003kn (at −7 days, $z = 0.244$) and SN 2003jt (at +3 days, $z = 0.45$). In Figure 13 we show a time sequence of the Ca II λ3945 region for a subset of the local and high-z SN Ia samples, identifying the blue and red absorption components and showing the good correspondence between profile shapes.

In Figure 14 (*top*) we show the evolution of $v_{\rm abs}$ for single- and double-absorption features in Ca II λ3945, selecting objects with $1.0 \leq \Delta m_{15}(B) \leq 1.7$; the value of the blue (red) component $v_{\rm blue}$ ($v_{\rm red}$) is systematically more (less) negative than single-absorption $v_{\rm abs}$ values at the same phase, perhaps caused by overlap with Si II λ3858. The blue and red data points for the high-z object (SN 2003kn) are consistent with the local SN Ia sample, although significantly shifted to more negative velocities and closer together (∼7000 rather than ∼10,000 km s^{-1}); more observations are needed to draw a firm conclusion. In Figure 14 (*bottom*) we show data points for objects with $\Delta m_{15}(B) < 1.0$. Only 1 (SN 1999aa) out of 10 local slow-declining SNe Ia shows such a double-absorption Ca II feature; 1 high-z fast-declining SN Ia (SN 2003jt) out of 17 (Fig. 13) also clearly displays this feature.

Contrary to the $1.0 \leq \Delta m_{15}(B) \leq 1.7$ objects, the blue component of Ca II λ3945 double absorptions in SN 1999aa does not correspond to a more negative $v_{\rm abs}$ than for the single absorptions. The red component, however, lies at significantly less negative $v_{\rm abs}$ (∼10,000 km s^{-1} greater than $v_{\rm abs}$ for the single-absorption features at similar phases). The approximately −5000 km s^{-1} vertical offset for SN 2003jt (Fig. 13) is clearly seen, although we are lacking local SNe Ia with Ca II λ3945 double-absorption features at these phases. Slow decliners are often associated with more luminous events (although not necessarily; see Table 2), which result from more energetic explosions (Mazzali et al. 1998; Leibundgut 2000). It would be worthwhile to study this spectral range in a large sample of local slow-declining SNe Ia in order to link the presence/absence of this feature with the kinematics, and thus kinetic energy, of the explosion. We note the absence of Ca II λ3945 double absorption in our sample of fast-declining SNe Ia [four SNe Ia with $\Delta m_{15}(B) > 1.7$].

Finally, selecting the five local SNe Ia of our sample (SN 1994D, 1996X, 1998aq, 1998bu, and 1999aa) having the best temporal coverage, we show in Figure 15 the evolution of the ratio $v_{\rm blue}/v_{\rm red}$. The nonunity, as well as the linear decline (except for SN 1994D), of $v_{\rm blue}/v_{\rm red}$ over ∼2 weeks seems difficult to reconcile with the presence of an inhomogeneity, expected to leave a more transient imprint.

4. CONCLUSIONS

No major systematic differences in the spectral evolution of absorption and emission-peak velocities of several prominent lines can be seen between local and high-z SN Ia spectra.

We present a robust measurement technique (§ 2.1), which is applied to both local and high-z SN Ia spectra. We also elaborate a reliable, if limited, error model (errors due to blending of spectral features cannot be reliably included). We use a spectral-smoothing algorithm that takes into account the Doppler broadening of SN Ia spectral features due to the large velocities in the ejecta, as well as the wavelength-dependent noise affecting ground-based spectra. Our line-profile analysis reduces the impact of line overlap, since it relies on a smaller wavelength interval, and allows for

asymmetric line profiles. The source code is available via the ESSENCE Web site[22] as both an IDL function and a FORTRAN script. All the results of our measurements are displayed in Tables 5–8.

We find both the magnitude and time evolution of v_{abs} for SNe Ia with different decline-rate parameters $\Delta m_{15}(B)$ to be consistent out to $z = 0.64$. As expected, strong lines have more negative absorption velocities, and weaker lines are better tracers of the decline-rate parameter, since they form over less extended regions. In fact, the S II $\lambda\lambda$5454, 5640 features can be used as diagnostic tools to separate fast-declining SNe Ia [$\Delta m_{15}(B) > 1.7$] from the rest, given a reliable phase. The lack of fast-declining SNe Ia in our high-z sample prevents us from assessing the validity of such a diagnostic at high redshifts. Most probably, the magnitude selection in ESSENCE prevents us from finding the intrinsically less luminous, fast-declining SNe Ia at higher redshift (Krisciunas et al. 2005).

For the first time, we present a census of peak emission velocities, found, up to 20 days past maximum B-band light, to be systematically negative. Such a blueshifted emission peak for the three studied lines is present in all SNe Ia of our local and high-z samples, regardless of their decline-rate parameter. We measure the v_{peak} associated with this blueshift and find it to be a significant fraction of v_{abs} for the S II λ5454 feature. We show that v_{peak} for the S II λ5454 feature can also be used to distinguish SNe Ia with $\Delta m_{15}(B) > 1.7$ at postmaximum phases, again given a reliable SN phase. Using a CMFGEN model (Hillier & Miller 1998), we illustrate the line-profile formation mechanisms in SNe Ia and show that this blueshifted emission stems from the steep density profile prevalent in SN atmospheres (Dessart & Hillier 2005a).

We report the detection of double-absorption Ca II λ3945 features in several local SNe Ia and for the first time confirm their detection in two high-z SNe Ia ($z = 0.244$ and 0.45; Fig. 13). The association of the blue component of this double absorption with Ca II is still under debate and could be due to contamination by Si II λ3858 (Gerardy et al. 2004).

The present investigation has not only shown the importance of such quantitative studies in assessing systematic differences between local and high-z SNe Ia but also makes a strong case for the need for higher quality SN Ia spectral data at high redshifts. From the first high-z spectrum of a SN Ia ever obtained (at $z = 0.31$; Nørgaard-Nielsen et al. 1989), previous and ongoing high-z SN Ia surveys have gathered sufficient data for detailed quantitative comparisons to be made between the two samples. To make the assertion of no evolution in the SN Ia sample with redshift, one would need a few high-quality SN Ia spectra, preferably with an $\sim$5 days sampling in rest-frame phase (i.e., an $\sim$1 week sampling at $z \approx 0.5$). This could ideally be done with the *Hubble Space Telescope* but could also be attempted with ground-based 8–10 m class telescopes (Matheson et al. 2005). Since the redshift uncertainty is the dominant source of error for our high-z measurements (when the redshift is determined from the SN itself), it is important for future studies of absorption and emission-peak velocities in SNe Ia to obtain a spectrum of the host galaxy along with that of the SN.

The ESSENCE high-z SN Ia spectra analyzed in this paper and initially presented in Matheson et al. (2005) are now publicly available.

The ESSENCE project is supported primarily by grants AST 02-06329 and AST 04-43378 from the US National Science Foundation (NSF). S. B. would like to thank Nando Patat and Paolo Mazzali for useful discussions on SN Ia spectral features and spectral synthesis. Darrin Casebeer's help in installing and running SYNOW is also greatly appreciated. S. B. acknowledges support from the International Max Planck Research School on Astrophysics via a graduate fellowship. A. V. F. is grateful for the support of NSF grant AST 03-07894 and for a Miller Research Professorship at the University of California, Berkeley, during which part of this work was completed.

[22] See http://www.ctio.noao.edu/essence.

REFERENCES

Barbon, R., Benetti, S., Rosino, L., Cappellaro, E., & Turatto, M. 1990, A&A, 237, 79
Barris, B. J., et al. 2004, ApJ, 602, 571
Benetti, S., et al. 2004, MNRAS, 348, 261
———. 2005, ApJ, 623, 1011
Blondin, S., Walsh, J. R., Leibundgut, B., & Sainton, G. 2005, A&A, 431, 757
Bolte, M., Saddlemyer, L., Mendes de Oliveira, C., & Hodder, P. 1989, PASP, 101, 921
Branch, D. 1977, MNRAS, 179, 401
Branch, D., Baron, E., Hall, N., Melakayil, M., & Parrent, J. 2005, PASP, 117, 545
Branch, D., Lacy, C. H., McCall, M. L., Sutherland, P. G., Uomoto, A., Wheeler, J. C., & Wills, B. J. 1983, ApJ, 270, 123
Branch, D., et al. 2003, AJ, 126, 1489
Coil, A. L., et al. 2000, ApJ, 544, L111
Dessart, L., & Hillier, D. J. 2005a, A&A, 437, 667
———. 2005b, A&A, 439, 671
Filippenko, A. V. 1997, ARA&A, 35, 309
———. 2004, in Measuring and Modeling the Universe, ed. W. L. Freedman (Cambridge: Cambridge Univ. Press), 270
———. 2005, in White Dwarfs: Cosmological and Galactic Probes, ed. E. M. Sion, S. Vennes, & H. L. Shipman (Dordrecht: Springer), 97
Filippenko, A. V., et al. 1992a, AJ, 104, 1543
———. 1992b, ApJ, 384, L15
Fisher, A., Branch, D., Hatano, K., & Baron, E. 1999, MNRAS, 304, 67
Fisher, A., Branch, D., Nugent, P., & Baron, E. 1997, ApJ, 481, L89
Frogel, J. A., Gregory, B., Kawara, K., Laney, D., Phillips, M. M., Terndrup, D., Vrba, F., & Whitford, A. E. 1987, ApJ, 315, L129
Garavini, G., et al. 2004, AJ, 128, 387
Garnavich, P. M., et al. 2004, ApJ, 613, 1120
Gerardy, C. L., et al. 2004, ApJ, 607, 391
Goldhaber, G., et al. 2001, ApJ, 558, 359
Gómez, G., López, R., & Sánchez, F. 1996, AJ, 112, 2094
Hamuy, M., et al. 2002a, AJ, 124, 417
———. 2002b, AJ, 124, 2339
Hatano, K., Branch, D., Fisher, A., Baron, E., & Filippenko, A. V. 1999, ApJ, 525, 881
Hernandez, M., et al. 2000, MNRAS, 319, 223
Hillebrandt, W., & Niemeyer, J. C. 2000, ARA&A, 38, 191
Hillier, D. J., & Miller, D. L. 1998, ApJ, 496, 407
Höflich, P. 1995, ApJ, 443, 89
Höflich, P., Müller, E., & Khokhlov, A. 1993, A&A, 268, 570
Höflich, P., Wheeler, J. C., & Thielemann, F.-K. 1998, ApJ, 495, 617
Höflich, P., et al. 2003, in Stellar Candles for the Extragalactic Distance Scale, ed. D. Alloin & W. Gieren (Berlin: Springer), 203
Horne, K. 1986, PASP, 98, 609
Howell, D. A., Höflich, P., Wang, L., & Wheeler, J. C. 2001, ApJ, 556, 302
Jeffery, D. J., & Branch, D. 1990, in Jerusalem Winter School for Theoretical Physics: Supernovae, ed. J. C. Wheeler, T. Piran, & S. Weinberg (Singapore: World Scientific), 149
Jha, S. 2002, Ph.D. thesis, Harvard Univ.
Jha, S., Riess, A. G., & Kirshner, R. P. 2006, ApJ, submitted
Jha, S., et al. 1999, ApJS, 125, 73
Kasen, D., Branch, D., Baron, E., & Jeffery, D. 2002, ApJ, 565, 380
Kasen, D., et al. 2003, ApJ, 593, 788
King, D. L., Vladilo, G., Lipman, K., de Boer, K. S., Centurion, M., Moritz, P., & Walton, N. A. 1995, A&A, 300, 881
Kirshner, R. P., & Kwan, J. 1974, ApJ, 193, 27

Kirshner, R. P., Oke, J. B., Penston, M. V., & Searle, L. 1973, ApJ, 185, 303
Kirshner, R. P., et al. 1993, ApJ, 415, 589
Knop, R. A., et al. 2003, ApJ, 598, 102
Krisciunas, K., Hastings, N. C., Loomis, K., McMillan, R., Rest, A., Riess, A. G., & Stubbs, C. 2000, ApJ, 539, 658
Krisciunas, K., Phillips, M. M., & Suntzeff, N. B. 2004a, ApJ, 602, L81
Krisciunas, K., et al. 2004b, AJ, 128, 3034
———. 2005, AJ, 130, 2453
Kurucz, R. L., & Bell, B. 1995, Kurucz CD-ROM 23, Atomic Line Data (Cambridge: SAO)
Leibundgut, B. 2000, A&A Rev., 10, 179
———. 2001, ARA&A, 39, 67
Leibundgut, B., Kirshner, R. P., Filippenko, A. V., Shields, J. C., Foltz, C. B., Phillips, M. M., & Sonneborn, G. 1991, ApJ, 371, L23
Leibundgut, B., & Sollerman, J. 2001, Europhysics News, 32, 4
Leibundgut, B., et al. 1993, AJ, 105, 301
———. 1996, ApJ, 466, L21
Lentz, E. J., Baron, E., Branch, D., Hauschildt, P. H., & Nugent, P. E. 2000, ApJ, 530, 966
Li, W., Filippenko, A. V., Treffers, R. R., Riess, A. G., Hu, J., & Qiu, Y. 2001a, ApJ, 546, 734
Li, W., et al. 2001b, PASP, 113, 1178
Li, W. D., et al. 1999, AJ, 117, 2709
Lidman, C. 2004, Messenger, 118, 24
Matheson, T., et al. 2005, AJ, 129, 2352
Mattila, S., Lundqvist, P., Sollerman, J., Kozma, C., Baron, E., Fransson, C., Leibundgut, B., & Nomoto, K. 2005, A&A, 443, 649
Mazzali, P. A. 2001, MNRAS, 321, 341
Mazzali, P. A., Cappellaro, E., Danziger, I. J., Turatto, M., & Benetti, S. 1998, ApJ, 499, L49
Mazzali, P. A., et al. 2005, ApJ, 623, L37
McElroy, D. B. 1995, ApJS, 100, 105
Meikle, W. P. S., et al. 1996, MNRAS, 281, 263
Nørgaard-Nielsen, H. U., Hansen, L., Jorgensen, H. E., Aragon Salamanca, A., & Ellis, R. S. 1989, Nature, 339, 523
Patat, F., Benetti, S., Cappellaro, E., Danziger, I. J., Della Valle, M., Mazzali, P. A., & Turatto, M. 1996, MNRAS, 278, 111
Perlmutter, S., et al. 1999, ApJ, 517, 565
Phillips, M. M. 1993, ApJ, 413, L105
Phillips, M. M., Lira, P., Suntzeff, N. B., Schommer, R. A., Hamuy, M., & Maza, J. 1999, AJ, 118, 1766
Phillips, M. M., Wells, L. A., Suntzeff, N. B., Hamuy, M., Leibundgut, B., Kirshner, R. P., & Foltz, C. B. 1992, AJ, 103, 1632
Phillips, M. M., et al. 1987, PASP, 99, 592
Pinto, P. A., & Eastman, R. G. 2000, ApJ, 530, 757
Prieto, J. L., Rest, A., & Suntzeff, N. B. 2006, ApJ, submitted
Prinja, R. K., Barlow, M. J., & Howarth, I. D. 1990, ApJ, 361, 607
Pritchet, C. J. 2005, in ASP Conf. Ser. 339, Observing Dark Energy, ed. S. C. Wolff & T. R. Lauer (San Francisco: ASP), 60
Riess, A. G., Press, W. H., & Kirshner, R. P. 1996, ApJ, 473, 88
Riess, A. G., et al. 1998, AJ, 116, 1009
———. 1999a, AJ, 117, 707
———. 1999b, AJ, 118, 2675
———. 2004, ApJ, 607, 665
Ruiz-Lapuente, P., Cappellaro, E., Turatto, M., Gouiffes, C., Danziger, I. J., Della Valle, M., & Lucy, L. B. 1992, ApJ, 387, L33
Sadakane, K., et al. 1996, PASJ, 48, 51
Saha, A., Sandage, A., Tammann, G. A., Dolphin, A. E., Christensen, J., Panagia, N., & Macchetto, F. D. 2001, ApJ, 562, 314
Salvo, M. E., Cappellaro, E., Mazzali, P. A., Benetti, S., Danziger, I. J., Patat, F., & Turatto, M. 2001, MNRAS, 321, 254
Schlegel, D. J., Finkbeiner, D. P., & Davis, M. 1998, ApJ, 500, 525
Spyromilio, J., Pinto, P. A., & Eastman, R. G. 1994, MNRAS, 266, L17
Stehle, M., Mazzali, P. A., Benetti, S., & Hillebrandt, W. 2005, MNRAS, 360, 1231
Stritzinger, M., et al. 2002, AJ, 124, 2100
Tonry, J. L., et al. 2003, ApJ, 594, 1
Turatto, M., Benetti, S., Cappellaro, E., Danziger, I. J., Della Valle, M., Gouiffes, C., Mazzali, P. A., & Patat, F. 1996, MNRAS, 283, 1
Turatto, M., Piemonte, A., Benetti, S., Cappellaro, E., Mazzali, P. A., Danziger, I. J., & Patat, F. 1998, AJ, 116, 2431
Vinkó, J., Kiss, L. L., Csák, B., Furész, G., Szabó, R., Thomson, J. R., & Mochnacki, S. W. 2001, AJ, 121, 3127
Vinkó, J., Kiss, L. L., Thomson, J., Furész, G., Lu, W., Kaszás, G., & Balog, Z. 1999, A&A, 345, 592
Wang, L., Wheeler, J. C., & Höflich, P. 1997, ApJ, 476, L27
Wang, L., et al. 2003, ApJ, 591, 1110
Wells, L. A., & Lee, M. G. 1995, AJ, 110, 1440
Wells, L. A., et al. 1994, AJ, 108, 2233